

# FedDyMem: Efficient Federated Learning with Dynamic Memory and Memory-Reduce for Unsupervised Image Anomaly Detection

Silin Chen  <sup>1</sup>, Andy Liu  <sup>1</sup>, Kangjian Di  <sup>1</sup>, Yichu Xu<sup>2,3</sup>, Han-Jia Ye  <sup>2,3</sup>,  
Wenhan Luo  <sup>4</sup>, Ningmu Zou  <sup>1,5\*</sup>

<sup>1</sup>School of Integrated Circuits, Nanjing University, Suzhou, 215163, Jiangsu, China.

<sup>2</sup>National Key Laboratory for Novel Software Technology, Nanjing University, Nanjing, 210023, Jiangsu, China.

<sup>3</sup>School of Artificial Intelligence, Nanjing University, Nanjing, 210023, Jiangsu, China.

<sup>4</sup>Hong Kong University of Science and Technology, Hong Kong.

<sup>5</sup>Interdisciplinary Research Center for Future Intelligent Chips (Chip-X), Nanjing University, Suzhou, 215163, Jiangsu, China.

\*Corresponding author(s). E-mail(s): [nzou@nju.edu.cn](mailto:nzou@nju.edu.cn);

Contributing authors: [silin.chen@mail.nju.edu.cn](mailto:silin.chen@mail.nju.edu.cn); [andyliu@mail.nju.edu.cn](mailto:andyliu@mail.nju.edu.cn);

[kangjiandi@mail.nju.edu.cn](mailto:kangjiandi@mail.nju.edu.cn); [xuyc@lamda.nju.edu.cn](mailto:xuyc@lamda.nju.edu.cn); [yehj@lamda.nju.edu.cn](mailto:yehj@lamda.nju.edu.cn);

[whluo.china@gmail.com](mailto:whluo.china@gmail.com);

## Abstract

Unsupervised image anomaly detection (UAD) has become a critical process in industrial and medical applications, but it faces growing challenges due to increasing concerns over data privacy. The limited class diversity inherent to one-class classification tasks, combined with distribution biases caused by variations in products across and within clients, poses significant challenges for preserving data privacy with federated UAD. Thus, this article proposes an efficient federated learning method with dynamic memory and memory-reduce for unsupervised image anomaly detection, called FedDyMem. Considering all client data belongs to a single class (i.e., normal sample) in UAD and the distribution of intra-class features demonstrates significant skewness, FedDyMem facilitates knowledge sharing between the client and server through the client's dynamic memory bank instead of model parameters. In the local clients, a memory generator and a metric loss are employed to improve the consistency of the feature distribution for normal samples, leveraging the local model to update the memory bank dynamically. For efficient communication and data privacy, a memory-reduce method based on weighted averages is proposed to significantly decrease the scale of memory banks. This reduced representation inherently, thereby mitigating the risk of data reconstruction. On the server, global memory is constructed and distributed to individual clients through k-means aggregation. Experiments conducted on six industrial and medical datasets, comprising a mixture of six products or health screening types derived from eleven public datasets, demonstrate the effectiveness of FedDyMem.

## 1 Introduction

Unsupervised image anomaly detection has achieved significant success in various domains, such as industrial inspection (Xie et al. (2024)) and medical disease recognition (Cai et al. (2024)). However, these methods highly depend on the availability of large-scale datasets for centralized training. Industrial companies and healthcare organizations often have practical limitations in collecting and aggregating raw data, which significantly challenges centralized learning approaches (Yang et al. (2024); Wu et al. (2024)). Recently, federated learning has been developed as a privacy-preserving paradigm for machine learning, providing collaborative model training across distributed devices while maintaining raw data locally and not transmitting to central servers (Li and Zhan (2021); Saha et al. (2024)). Thus, the integration of local training and global aggregation strategies has garnered significant attention in industrial and healthcare domains, enabling data privacy protection (Zhao et al. (2024); Zhang et al. (2024d)).

Federated learning is applicable to both supervised and unsupervised learning scenarios. Recent developments in unsupervised and semi-supervised federated learning have shown significant progress (Jin et al. (2023); Yang et al. (2025)). These methods are often focused on learning a general representation or prototype by self-supervised learning (SSL) while keeping private data decentralized and unlabeled. Some methods continue to rely on local updates and aggregation of model parameters to train a global model for representation generation (Zhuang et al. (2021); Liao et al. (2024)). Alternatively, other approaches take advantage of representation sharing, using knowledge distillation (KD) to construct a robust representation space (Han et al. (2022); Lubana et al. (2022); Zhang et al. (2024a)). However, these methods are designed to obtain a more efficient representation by SSL and require local fine-tuning through a supervised linear evaluation protocol (Zhuang et al. (2021)) following federated learning. Consequently, existing approaches

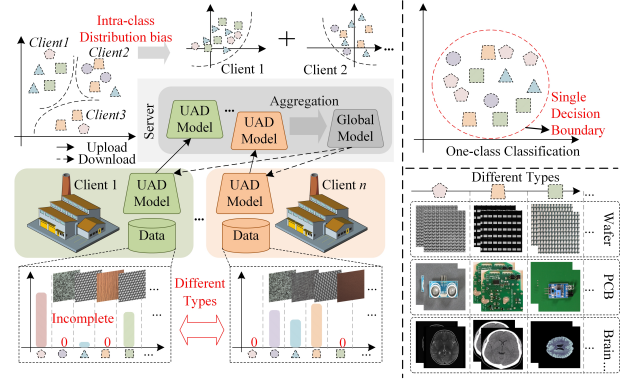


**Fig. 1** Illustration of federated learning in UAD. As shown on the left, for the same product anomaly detection, an intra-class distribution bias exists between local models, caused by each client possessing varying and incomplete subsets of product types. As shown in the top right, federated UAD aims to establish a single decision boundary for one-class classification within the global model. Examples of type differences in anomaly detection for different products are shown in the right down.

in unsupervised federated learning are inadequate for addressing the UAD task.

With the advancements in UAD using deep learning, reconstruction-based methods (Liang et al. (2023); Dai et al. (2024)) have emerged as prominent strategies by learning to accurately reconstruct normal samples while minimizing reconstruction loss, thereby enabling the identification of anomalies as deviations from expected reconstructions. Intuitively, integrating reconstruction loss functions to locally optimize the model, followed by aggregating the model weights through federated learning approaches, presents a promising avenue for enabling federated learning in UAD. However, as shown in Fig. 1, the intra-class distribution bias within the normal sample class, caused by variations in products, is also an important issue in UAD (Lei et al. (2025)). Similarly, data heterogeneity in federated learning can lead to significant performance degradation and convergence challenges, primarily due to inconsistencies in local updates and optimization dynamics (Karimireddy et al. (2020); Zhao et al. (2018)). Recently, most of the current federated learning methods focus

on addressing the challenges posed by data heterogeneity (Li et al. (2020b, 2021b, 2022); Zhou et al. (2024); Dai et al. (2023)). To address the feature shift challenge in federated learning, some methods have proposed incorporating local constraints by the global model or gradient information, thereby mitigating discrepancies across clients (Li et al. (2020b, 2021b); Karimireddy et al. (2020); Luo and Wu (2022)). Despite these efforts, the significant intra-class feature distribution bias in UAD results in insufficient global information to effectively capture the representations and knowledge of diverse products (Huang et al. (2023)). Meanwhile, other researchers have addressed this issue by synthesizing data (Nguyen et al. (2021); Li et al. (2024b)). However, sharing additional data among clients inherently increases the risk of data privacy leakage (Li et al. (2024a)). Recent approaches have increasingly emphasized prototype-learning methods to tackle the challenges posed by inconsistent data distributions. These methods construct category-specific global and local prototypes by leveraging feature alignment, effectively addressing generalization gaps across local clients (Tan et al. (2022a); Zhang et al. (2024b); Dai et al. (2023); Zhou et al. (2024)). Nevertheless, reconstruction-based loss functions in UAD often lead to overfitting on local features of normal samples (You et al. (2022)). The use of a single category hinders effective global feature aggregation and prevents normal representations from achieving a compact distribution. As a result, the aggregated prototypes deviate from the desired global distribution of normal samples.

Furthermore, communication between clients in federated learning is limited by network bandwidth, unreliable connections, and varying device statuses. Consequently, designing communication-efficient algorithms is crucial to overcome these challenges (Almanifi et al. (2023)). Existing methods primarily tackle this issue by either decreasing the total number of communication rounds required for model convergence or reducing the data uploaded during each communication round (Li et al. (2020a)). To accelerate global convergence, some approaches leverage mechanisms such as localized model updates (Li et al. (2020c)) and gradient optimization enhancements (Yang et al. (2022)), effectively reducing the number of communication rounds. To reduce the

data uploaded, methods such as model compression (Shlezinger et al. (2020); Li et al. (2023a)) and selective client participation (Xu and Wang (2020)) have been extensively explored to minimize communication overhead. Beyond efficiency, privacy-ensured communication is equally essential, especially in resource-constrained and privacy-sensitive environments. The exchanged information should resist reconstruction attempts from adversaries, preventing leakage of the raw client data (Cao et al. (2025)). In this article, we aim to minimize simultaneously communication overhead and the mutual information with the original data through effective data reduction techniques, thereby improving the communication efficiency and enhancing privacy protection.

To summarize, federated UAD must address the following key challenges: 1) enabling each client to perform end-to-end unsupervised anomaly detection without the reliance on additional labeled data or supervised fine-tuning, utilizing only one-class (normal) samples as the basis for training. 2) mitigating significant distribution biases in normal sample data across clients, which arise due to the heterogeneous product types or health screening modalities within the federated learning framework. 3) ensuring communication between clients and the central server is both privacy-preserving and communication-efficient. This article introduces FedDyMem, an efficient federated learning framework with dynamic memory and memory-reduce, specifically designed to tackle the aforementioned challenges in federated UAD. FedDyMem facilitates knowledge transfer in federated learning by sharing the memory bank instead of model parameters among clients. Specifically, it constructs a local memory bank using the limited dataset of normal samples available at each client. To address the challenge of intra-class distribution bias in different clients, a memory generator and a metric loss function are introduced to improve the consistency of normal feature distributions. Then the local memory bank is dynamically updated by the local client model before uploading. To mitigate distribution bias during aggregation, FedDyMem employs k-means clustering to extract general distribution from different clients, thereby ensuring effective aggregation without confusion. Considering communication efficiency and data privacy, a memory-reduce method is proposed to decrease

the scale of memory banks, thereby reducing its mutual information with the original data during dynamic updates. To construct diverse data for our experiments, we categorize the 11 public datasets into six distinct types based on their inherent characteristics. We then evaluate our proposed method separately on six product or health screening types, achieving state-of-the-art performance in each case. The major contributions of this article are summarized as follows:

- To the best of our knowledge, FedDyMem is the first federated learning framework designed specifically for unsupervised image anomaly detection. This framework facilitates collaborative training using only normal samples available on the client side.
- To address the significant distribution biases of normal samples across clients, we incorporate a memory generator and a metric loss function that improve the consistency of feature distributions. Additionally, we employ k-means clustering during the aggregation phase to reduce inter-client discrepancies and mitigate potential ambiguities.
- To achieve both communication efficiency and privacy-preserving knowledge sharing, we propose a memory-reduce method based on a dynamic weighted average. This method substantially decreases the size of the memory bank, thereby reducing both communication overhead and the mutual information between uploaded information and raw data, while preserving model performance.
- We have collected eleven image anomaly detection datasets from various industrial and medical domains. These datasets are further divided into six datasets depending on the type of product or health screening. Comprehensive experiments demonstrate that FedDyMem achieves excellent federated UAD performance.

## 2 Related Work

### 2.1 Unsupervised Image Anomaly Detection

The objective of UAD is to identify whether a given sample is anomalous and to precisely localize the anomaly regions, using a training dataset

that comprises only normal samples (Xie et al. (2024)). The reconstruction-based methods are significant in UAD, which assumes that anomalous samples cannot be accurately reconstructed by feature learning models trained exclusively on normal samples (Bergmann et al. (2018); Zavrtanik et al. (2021); Jiang et al. (2022); Liang et al. (2023); Dai et al. (2024)). In contrast to traditional UAD approaches, which rely on a single, centralized training dataset, federated UAD requires the efficient aggregation of information from samples distributed across multiple clients. Reconstruction-based methods, however, typically rely solely on normal samples within the training set and fail to capture key characteristics of out-of-distribution samples. Another widely utilized approach for anomaly detection is the memory bank-based method. SPADE (Cohen and Hoshen (2020)) proposed a semantic pyramid structure to construct a pixel-level feature memory, effectively facilitating anomaly detection. PaDiM (Defard et al. (2021)) employed Gaussian distributions derived from normal samples as the memory bank and utilized the Mahalanobis distance as the anomaly metric. PatchCore (Roth et al. (2022)) introduced local neighborhood aggregation to expand the receptive field of the memory bank while preserving resolution. Additionally, PatchCore implemented a greedy core-set subsampling strategy to reduce the memory bank size without significant performance degradation. PNI (Bae et al. (2023)) further advanced the paradigm by integrating spatial and neighborhood information into the memory bank construction, thereby improving its capacity to represent normal samples comprehensively. These methods extract features from normal images and store them within a feature memory bank. During testing, the sample queries the memory bank to retrieve feature corresponding to the k-nearest neighbors. However, the memory banks are non-trainable, limiting their capacity to learn information across local clients in the federated learning.

### 2.2 Federated Learning

The federated learning can be divided into supervised-based and unsupervised-based methods. In unsupervised federated learning, most existing methods focused on representation learning or prototype-based learning, which aimed to

learn good feature representations from unlabeled data to facilitate downstream machine learning tasks (Zhuang et al. (2021); Liao et al. (2024); Han et al. (2022); Lubana et al. (2022); Zhang et al. (2024a)). However, these methods depend on aligning local representations with global representations, a task that proves challenging for UADs constrained to a single category. ProtoFL (Kim et al. (2023)) was proposed to integrate federated learning with prototyping for addressing one-class classification. However, its two-stage fine-tuning method, which utilizes normalizing flow for representation learning, introduces unnecessary computational overhead and ignores distribution bias among clients in UAD. Furthermore, most unsupervised federated learning approaches require supervised fine-tuning, which limits their applicability to UAD.

FedAvg (McMahan et al. (2017)) is a foundational approach in federated learning that enables the training of a global model by aggregating parameters from locally trained models. Despite its effectiveness, the performance of FedAvg degrades significantly with high data heterogeneity. FedProx (Li et al. (2020b)) and SCAFFOLD (Karimireddy et al. (2020)) demonstrated enhanced performance through a global penalty term, effectively addressing and mitigating discrepancies. Other methods have now been developed to address the data heterogeneity with the personalized model. FedBN (Li et al. (2021b)) mitigates data heterogeneity challenges in federated learning by maintaining BN parameters that are specific to each client’s local model. APPLE (Luo and Wu (2022)) aggregates client models locally by learning precise weight updates instead of relying on approximations. Recent approaches address generalization gaps across local clients by leveraging feature alignment to construct category-specific global and local prototypes (Tan et al. (2022a); Dai et al. (2023); Zhou et al. (2024); Zhang et al. (2024b)). Nevertheless, the aforementioned methods face significant challenges in UAD, including high communication overhead, insufficient representation diversity and pronounced intra-class distribution bias.

### 3 Preliminary

#### 3.1 Typical Federated Learning

In the typical federated learning, such as FedAvg (McMahan et al. (2017)), there exist  $N$  clients  $\{\mathcal{C}_n\}_{n=1}^N$  with their individual datasets  $\{\mathcal{D}_n = (\mathcal{X}_n, \mathcal{Y}_n) \sim \mathbb{P}_n(\mathcal{X}, \mathcal{Y})\}_{n=1}^N$  and local models  $\{f^n(\cdot; \mathbf{W}^n) : \mathcal{X}_n \rightarrow \mathcal{Y}_n\}_{n=1}^N$ , where  $n$  is the index for the client,  $(\mathcal{X}_n, \mathcal{Y}_n)$  denotes a set of samples and labels on the  $n$ -th client,  $\mathbb{P}_n(\mathcal{X}, \mathcal{Y})$  represent the joint distribution of samples and labels. The objective of the typical federated learning is to facilitate collaborative training of a global model  $\mathbf{W}^G$  that generalizes effectively across the entire dataset  $\mathcal{D}$  while ensuring data privacy. The global training optimization target is:

$$\min_{\mathbf{W}^G} \mathcal{L}(\mathbf{W}^G) \triangleq \sum_{n=1}^N z_n \mathcal{L}_n(\mathbf{W}^n), \quad (1)$$

where the  $z_n$  denotes the weight coefficient which is computed as  $\frac{|\mathcal{D}_n|}{|\mathcal{D}|}$  in FedAvg, where the  $|\mathcal{D}| = \bigcup_{n=1}^N \mathcal{D}_n$ . The empirical loss  $\mathcal{L}_n(\mathbf{W}^n)$  of the  $n$ -th client can be formulated as:

$$\mathcal{L}_n(\mathbf{W}^n) = \mathbb{E}_{(x \in \mathcal{X}_n, y \in \mathcal{Y}_n) \sim \mathbb{P}_n(\mathcal{X}, \mathcal{Y})} [\ell(f^n(x; \mathbf{W}^n), y)], \quad (2)$$

where  $\ell(\cdot, \cdot)$  denotes the loss function on the clients. Following the local updates, the server  $\mathcal{S}$  performs aggregation of multiple local models’ parameters to derive the global model as  $\mathbf{W}^G \leftarrow \sum_{n=1}^N z_n \mathbf{W}^n$ .

#### 3.2 Federated UAD

As shown in Fig. 1, each client in UAD could be an industrial manufacturing enterprise, an organizational entity or a healthcare institution, etc. that faces the challenges of large raw abnormal data. Consequently, the training dataset available at the  $n$ -th client is denoted as:

$$\mathcal{D}_n^{train} = (\mathcal{X}_n, \mathcal{Y}_n) \sim \mathbb{P}_n(\mathcal{X}), \forall y \in \mathcal{Y}_n, y = 0, \quad (3)$$

and the test dataset is denoted as

$$\begin{aligned} \mathcal{D}^{test} &= \bigcup_{n=1}^N \mathcal{D}_n^{test}, \text{ where} \\ \mathcal{D}_n^{test} &= (\mathcal{X}_n, \mathcal{Y}_n) \sim \mathbb{P}_n(\mathcal{X}, \mathcal{Y}), \exists y \in \mathcal{Y}_n, y = 1, \end{aligned} \quad (4)$$

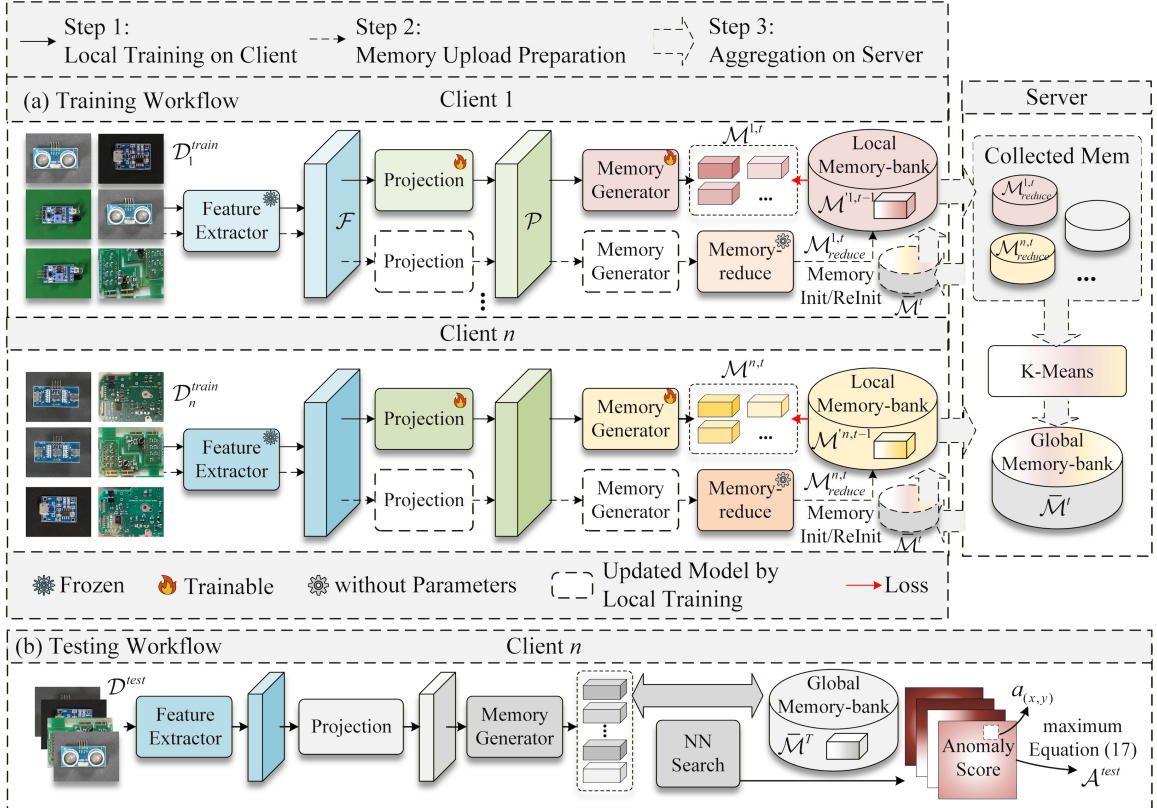


**Fig. 2** Overview of our proposed FedDyMem framework.

where a label  $y = 0$  indicates a normal sample, while  $y = 1$  denotes an anomalous sample. In practical scenarios, as shown in Fig. 1, the distribution of client samples for the same product is different in training dataset:

$$\exists_{x_m \in \mathcal{D}_m^{train}, x_n \in \mathcal{D}_n^{train}} \mathbb{P}_m(x_m) \neq \mathbb{P}_n(x_n), \text{ while } m \neq n. \quad (5)$$

We refer to this variation as the intra-class distribution bias. Consistent with typical federated learning, our global optimization objective remains as defined in 1. However, due to the absence of anomalous samples in the  $\mathcal{D}^{train}$ , the local model  $f^n(\cdot; \mathbf{W}^n)$  cannot effectively model  $\mathcal{X}_n \rightarrow \mathcal{Y}_n$ . Thus, the empirical loss of the  $n$ -th client in UAD is formulated as:

$$\mathcal{L}_n(\mathbf{W}^n) = \mathbb{E}_{(x \in \mathcal{X}_n) \sim \mathbb{P}_n(\mathcal{X})} [\ell(f^n(x; \mathbf{W}^n))], \quad (6)$$

where  $\ell(\cdot)$  denotes the local loss function for individual clients. It requires the  $n$ -th local model  $f^n(\cdot; \mathbf{W}^n)$  to approximate the normal sample distribution, i.e.,  $\mathbb{P}_n(\mathcal{X}^{train})$ , under the condition

of intra-class bias (refer to 5). For the federated UAD, shown in Fig. 1, the global model's objective in one-class classification task is to generalize across all clients by constructing  $\mathbb{P}(\{\mathcal{X}_n^{train}\}_{n=1}^N)$ . During the testing phase, the result of a sample  $x^{test} \in \mathcal{D}^{test}$  can be expressed as follows:

$$\mathbb{1}(x^{test}) = \begin{cases} 0, & \text{if } f(x^{test}; \mathbf{W}^G) \sim \mathbb{P}(\{\mathcal{X}_n^{train}\}_{n=1}^N) \\ 1, & \text{otherwise.} \end{cases} \quad (7)$$

## 4 Methodology

### 4.1 Overview

In this article, we propose an efficient federated learning with dynamic memory and memory-reduce for UAD, called FedDyMem. FedDyMem aims to train model parameters on datasets with locally inconsistent feature distributions and generate a global memory bank that produces uniform distributions, thereby achieving high performance on global  $\mathcal{D}^{test}$ . Each communication

round in FedDyMem comprises the following three steps of training: 1) Local training: On the  $n$ -th client, as shown in Fig. 2, the feature extractor, projection layer, and memory generator collaboratively generate high-quality memory representations  $\{\mathcal{M}^{n,i,t}\}_{i=0}^{|\mathcal{D}_n^{train}|}$  in the training workflow, where  $i$  denotes the  $i$ -th sample in  $\mathcal{D}_n^{train}$  and  $t$  denotes the  $t$ -th rounds. During the initialization phase ( $t = 0$ ), all memory features  $\{\mathcal{M}^{n,i,0}\}_{i=0}^{|\mathcal{D}_n^{train}|}$  extracted from training samples are processed through memory-reduce before being send directly to the server. The local memory bank  $\mathcal{M}^{n,0}$  synchronizes with the aggregated memory bank  $\bar{\mathcal{M}}^0 \xleftarrow{\text{agg}} \{\mathcal{M}^{n,0}_{\text{reduce}}\}_{n=0}^N$  received from the server. After initialization, the extracted memory feature for sample  $i$ , denoted as  $\mathcal{M}^{n,i,t}$ , is utilized in subsequent rounds to compute the local loss  $\ell$ . This computation is performed in conjunction with the local memory bank  $\mathcal{M}^{n,t-1}$ , which is obtained from the server aggregation during the previous round. 2) Memory preparation: After the local training step in each communication round, both the projection layer and the memory generator are updated. Subsequently, the local training samples are passed through the trained models to extract the corresponding memory features, denoted as  $\mathcal{M}^{n,i,t}$ . These per-sample memory features are then reduced by the memory-reduce, summarized as  $\{\mathcal{M}^{n,i,t}\}_{i=0}^{|\mathcal{D}_n^{train}|} \rightarrow \mathcal{M}_{\text{reduce}}^{n,t}$ . Representation sharing (Kim et al. (2023); Tan et al. (2022a); Zhang et al. (2024a)) provides distinct advantages over parameter aggregation in addressing heterogeneity in unsupervised federated learning, as parameter aggregation methods suffer from privacy and intellectual property (IP) concerns (Li et al. (2021a); Zhang et al. (2024c)) and introduce high communication overhead. Therefore, FedDyMem introduces the memory-reduce operation and the memory bank sharing mechanism to mitigate communication costs while preserving client data privacy. 3) Aggregation and distribution: In the  $t$ -th round, the server receives  $N$  local memory banks, denoted as  $\{\mathcal{M}_{\text{reduce}}^{n,t}\}_{n=0}^N$ . As shown in Fig. 2, FedDyMem employs  $K$ -means clustering algorithm, where  $K$  corresponds to the capacity of the local memory, to aggregate the diverse local memory banks into a unified global memory bank, represented as  $\bar{\mathcal{M}}^t \xleftarrow{\text{agg}} \{\mathcal{M}_{\text{reduce}}^{n,t}\}_{n=0}^N$ . The global

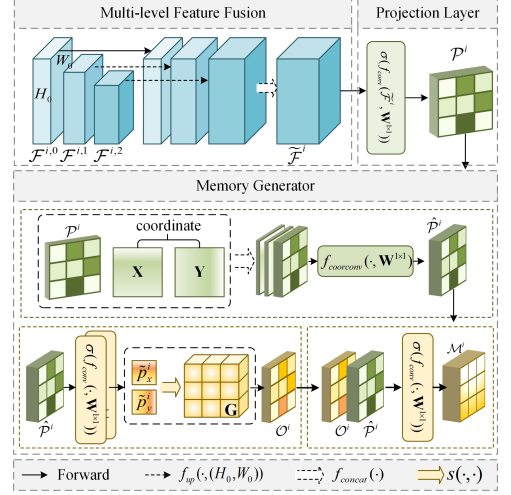


Fig. 3 Illustration of the feature extraction process in FedDyMem.

memory bank  $\bar{\mathcal{M}}^t$  is subsequently distributed to all clients to update their respective local memory banks. Consequently, at any round  $t$ , for all  $n \in N$ , the local memory banks are synchronized such that  $\mathcal{M}^{n,t} = \bar{\mathcal{M}}^t$ .

During the testing phase, the extracted memory features  $\mathcal{M}^i$  are compared against the memory bank  $\bar{\mathcal{M}}$  using the nearest neighbor search, and the anomaly score  $\mathcal{A}^i$  is computed based on the resulting metric, following the anomaly score function in (Roth et al. (2022); Lee et al. (2022)).

## 4.2 Methodology for Obtaining $\mathcal{M}^{n,i,t}$

Locally, FedDyMem employs a frozen CNN model  $\mathcal{F}(\cdot)$  pre-trained on ImageNet to extract multi-level hierarchical features. Motivated by (Roth et al. (2022)), FedDyMem performs multi-level feature fusion on the extracted features. As shown in Fig. 3, for a given sample  $x_i^n \in \mathbb{R}^{H \times W \times 3}$  which is from the  $n$ -th client's  $\mathcal{D}_n$ , the extracted features are hierarchically organized into  $L$  layers (e.g.,  $L = 5$  in the case of ResNet (He et al. (2016))). We define  $\mathcal{F}^{i,l} \in \mathbb{R}^{H_l \times W_l \times C_l}$  as the output features of the  $l$ -th layer, obtained from  $\mathcal{F}(x_i^n)$ , where  $i$  denotes the  $i$ -th sample from local dataset,  $l \in L$  denotes the  $l$ -th layer and  $H_l$ ,  $W_l$ ,  $C_l$  are the size and channel of the feature map. In multi-level feature fusion, we employ a straightforward approach combining up-sampling and feature concatenation to extract features from pre-trained CNNs. This

---

**Algorithm 1** Memory Generator for the sample  $x_i^n$  on Client  $n$  at Round  $t$ .

---

**Input:**  $n, t, x_i^n \in \mathcal{D}_n^{train}, \mathcal{F}(\cdot), \mathcal{P}^n(\cdot, \mathbf{W}^{\mathcal{P}}), \mathcal{G}^n(\cdot, \mathbf{W}^{\mathcal{G}}; \mathbf{G})$ .  
**Output:**  $\mathcal{M}^i$ .

- 1:  $\{\mathcal{F}^{(i,l)}\}_{l=1}^L \leftarrow \mathcal{F}(x_i^n)$ , where  $L$  is determined by  $\mathcal{F}$ ;
- 2:  $\tilde{\mathcal{F}}^i \leftarrow$  Compute by Equation (8);
- 3:  $\mathcal{P}^i \leftarrow$  Compute by Equation (9);
- 4:  $\mathcal{M}^i \leftarrow \mathcal{G}^n(\mathcal{P}^i, \mathbf{W}^{\mathcal{G}}; \mathbf{G})$  with Equation (10) (11);
- 5: **return**  $\mathcal{M}^i$

---

process can be expressed as follows:

$$\tilde{\mathcal{F}}^i = f_{concat}(\{f_{up}(\mathcal{F}^{i,l}, (H_0, W_0))\}_{l=0}^L), \quad (8)$$

where  $f_{concat}(\cdot)$  represents the concatenation operation,  $f_{up}(\cdot, (H, W))$  denotes bilinear interpolation to the spatial dimensions  $(H, W)$ . Feature extractors pretrained on large-scale natural image datasets often exhibit significant distribution shifts when applied to industrial or medical images. To address this issue, we introduce a projection layer  $\mathcal{P}(\cdot, \mathbf{W}^{\mathcal{P}})$  designed to adapt the extracted features to the anomaly detection domain. As shown in Fig. 3, the projection layer is implemented as a  $1 \times 1$  convolutional layer, enabling the output  $\mathcal{P}^i$  of the projection to be computed as follows:

$$\mathcal{P}^i = \sigma(f_{conv}(\tilde{\mathcal{F}}^i, \mathbf{W}^{1 \times 1})), \quad (9)$$

where  $f_{conv}(\cdot, \mathbf{W}^{q \times q})$  denotes  $q \times q$  convolution layer,  $\sigma(\cdot)$  denotes the activation function.

The memory bank-based approach (Cohen and Hoshen (2020); Defard et al. (2021); Roth et al. (2022)) has demonstrated significant performance in UAD. However, the memory banks utilized in these existing methods are non-trainable, meaning they remain unchanged following initialization. Due to the local bias in feature distributions for federated UAD, using the static memory bank will lead to overfitting on domain-specific data, increasing the risk of error. Furthermore, existing methods operate mainly on a discrete feature space, which increases the variations in feature distributions between clients for normal samples (Lee et al. (2025)). In this article, we

propose a memory generator that integrates spatial information and ensures the continuity of feature space. As shown in Fig. 3, the memory generator  $\mathcal{G}(\cdot, \mathbf{W}^{\mathcal{G}}; \mathbf{G})$  utilizes a coordinate convolution layer  $f_{coorconv}(\cdot, \mathbf{W}^{1 \times 1})$  to encode spatial location information by incorporating additional coordinate channels, thereby facilitating the network's ability to learn spatial transformations more effectively (Liu et al. (2018)). For the projected feature  $\mathcal{P}^i$ , the result of the coordinate convolution  $\hat{\mathcal{P}}^i \in \mathbb{R}^{H \times W \times C}$  is computed as  $\hat{\mathcal{P}}^i = f_{coorconv}(f_{concat}(\{\mathcal{P}^i, \mathbf{X}, \mathbf{Y}\}), \mathbf{W}^{1 \times 1})$ , where  $\mathbf{X}$  and  $\mathbf{Y}$  represent the Cartesian coordinates of the feature map. Then, to enhance the continuity of the memory bank, the memory generator utilizes a grid-based approach to construct a continuous feature space. We define a trainable grid space as  $\mathbf{G} \in \mathbb{R}^{H^{\mathbf{G}} \times W^{\mathbf{G}} \times C}$ , where  $H^{\mathbf{G}}$  and  $W^{\mathbf{G}}$  are hyperparameters indicating the size of the continuous space. The memory generator maps  $\hat{\mathcal{P}}^i$  to pixel-wise coordinates  $\tilde{\mathcal{P}}^i \in \mathbb{R}^{H \times W \times 2}$  through a mapping function  $\phi(\cdot, \mathbf{W}) : \mathbb{R}^{H \times W \times C} \rightarrow \mathbb{R}^{H \times W \times 2}$ , implemented through two  $1 \times 1$  convolutional layers in our memory generator. A sample function  $s(\cdot, \cdot)$  is employed to extract features from the continuous space  $\mathbf{G}$  at specific coordinate values  $(p_x^i, p_y^i) \in \tilde{\mathcal{P}}^i$ . The normalized coordinates are computed as follows:

$$\tilde{p}_x^i = \frac{(p_x^i + 1)}{2} \cdot (W^{\mathbf{G}} - 1), \quad \tilde{p}_y^i = \frac{(p_y^i + 1)}{2} \cdot (H^{\mathbf{G}} - 1), \quad (10)$$

and the result of  $s(\mathbf{G}, \tilde{\mathcal{P}}^i)$  is defined as  $\mathcal{O}^i$ . Each pixel value in  $\mathcal{O}^i$  can be sampled as:

$$\mathcal{O}_{xy}^i = \sum_{m=0}^{1} \sum_{n=0}^{1} w_{mn} \mathbf{G}_{\lfloor \tilde{p}_y^i \rfloor + m, \lfloor \tilde{p}_x^i \rfloor + n}, \text{ where } (11)$$

$$w_{mn} = (1 - |\tilde{p}_x^i - (\lfloor \tilde{p}_x^i \rfloor + n)|)(1 - |\tilde{p}_y^i - (\lfloor \tilde{p}_y^i \rfloor + m)|),$$

where  $\lfloor \cdot \rfloor$  represents the floor operation. Finally, the features  $\mathcal{O}^i$ , sampled from the continuous feature space, are concatenated with the coordinate convolution outputs  $\hat{\mathcal{P}}^i$ . This concatenated tensor is then passed through a convolutional layer to generate the memory feature  $\mathcal{M}^i \in \mathbb{R}^{H \times W \times C}$  for client  $n$  at round  $t$ . The complete procedure for obtaining the memory feature is presented in Algorithm 1.

### 4.3 Computation of Local Metric Loss: $\ell(\mathcal{M}^{n,i,t}, \mathcal{M}'^{n,t-1})$

Considering the bias in feature distributions across clients, the training objective is to optimize the local memory generator to produce normal features that are more closely aligned with the shared global memory bank. FedDyMem introduces a simple metric loss to optimize the parameters of both the memory generator and the projection layer, thereby facilitating client models in generating consistent and high-quality memory features. Specifically, the local memory bank for round  $t$  is denoted as  $\mathcal{M}'^{n,t-1} = \{m'_d\}_{d=0}^{H \times W} \in \mathbb{R}^{(H \times W) \times C}$ , where its size is reduced to  $H \times W$  after the initialization on the  $n$ -th client and global aggregation by the server (details of memory-reduce and aggregation are provided in Section 4.4 and Section 4.5). Similar to the patch-based memory bank, the memory features  $\mathcal{M}^{n,i,t}$  can be expressed as a collection of patch features,  $\{m_{(h,w)} \in \mathbb{R}^C\}_{h=0,w=0}^{H,W}$ . The loss function  $\ell$  is defined as follow:

$$\begin{aligned} & \ell(\mathcal{M}^{n,i,t}, \mathcal{M}'^{n,t-1}) \\ &= \frac{1}{HWK} \sum_{h,w}^{H,W} \sum_k^K \max(0, \text{dis}(m_{(h,w)}, m'_k) - th), \end{aligned} \quad (12)$$

where the function  $\text{dis}(\cdot, \cdot)$  represents the Euclidean distance metric in this article,  $th$  is a hyperparameter to mitigate overfitting. Specifically, we employ a  $K$ -nearest neighbor (KNN) search to retrieve the top  $K$  closest features from the memory bank corresponding to the generated features. Therefore,  $k$  denotes the index in top  $K$ . FedDyMem uses the metric loss function to align the local features with the global memory bank. Following local training, the local memory bank is updated once before being uploaded to the server. This ensures that the local memory bank closely approximates the global memory bank in feature space.

### 4.4 Memory-reduce for

$$\{\mathcal{M}^{n,i,t}\}_{i=0}^{|\mathcal{D}_n^{\text{train}}|} \rightarrow \mathcal{M}_{\text{reduce}}^{n,t}$$

The earlier memory-based methods (Cohen and Hoshen (2020); Roth et al. (2022)) involved storing all sample memory features from the training

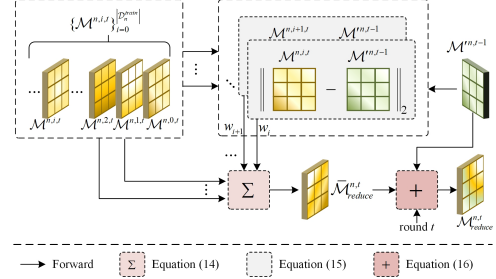


Fig. 4 Illustration of Memory-reduce.

dataset  $\mathcal{D}_n^{\text{train}}$  within the memory bank. Accordingly, the capacity of the memory bank scales proportionally with the size of the local dataset. For federated UAD, this design leads to high communication overhead when applied to large-scale datasets and also introduces privacy risks. When each memory feature corresponds directly to a raw input sample, it becomes vulnerable to privacy leakage under reconstruction or inversion attacks. Moreover, the varying sizes of memory banks also introduce challenges in the aggregation process. Motivated by this, FedDyMem incorporates a memory-reduce method to compress the collected memory features from the local dataset, thereby reducing the mutual information between the memory features and the raw data. The objective of memory-reduce can be expressed as follows:

$$\begin{aligned} & \{\mathcal{M}^{n,i,t}\}_{i=0}^{|\mathcal{D}_n^{\text{train}}|} \in \mathbb{R}^{|\mathcal{D}_n^{\text{train}}| \times H \times W \times C} \\ & \rightarrow \mathcal{M}_{\text{reduce}}^{n,t} \in \mathbb{R}^{H \times W \times C}, \end{aligned} \quad (13)$$

where  $\mathcal{M}^{n,i,t}$  represents the memory feature extracted by client  $n$  for the  $i$ -th sample in the training dataset  $\mathcal{D}_n^{\text{train}}$ ,  $H$  and  $W$  denote the spatial dimensions of the memory feature, and  $C$  indicates the number of feature channels.

To address the memory bank size issue, (Lee et al. (2022)) employs an Exponential Moving Average (EMA) method. However, the reduced memory bank remains sensitive to the sequence in which input samples are processed. In this article, we introduce a dynamic weighted average, called memory-reduce, that optimizes memory size while preserving sample order independence and effectively correlating with the number of communication rounds. As shown in Fig. 4, we aggregate all memory features, denoted as  $\{\mathcal{M}^{n,i,t}\}_{i=0}^{|\mathcal{D}_n^{\text{train}}|}$  and apply a dynamic weighted averaging operation to

---

**Algorithm 2** Memory Reduce for the  $\{\mathcal{M}^{n,i,t}\}_{i=0}^{\|\mathcal{D}_n^{\text{train}}\|}$  on Client  $n$  at Round  $t$ .

---

**Input:**  $n, t, \{\mathcal{M}^{n,i,t}\}_{i=0}^{\|\mathcal{D}_n^{\text{train}}\|}, \mathcal{M}'^{n,t-1}$ .

**Output:**  $\bar{\mathcal{M}}_{\text{reduce}}^{n,0}$ .

- 1: **for**  $i = 0$  to  $\|\mathcal{D}_n^{\text{train}}\|$  **do**
- 2:   **if**  $t > 0$  **then**
- 3:      $w_{i,t} \leftarrow$  Compute by Equation (15) with  $\mathcal{M}^{n,i,t}$  and  $\mathcal{M}'^{n,t-1}$ ;
- 4:     **else**
- 5:        $w_{i,t} \leftarrow 1$ ;
- 6:     **end if**
- 7: **end for**
- 8:  $\bar{\mathcal{M}}_{\text{reduce}}^{n,t} \leftarrow$  Compute by Equation (14) with  $\{w_{i,t}\}_{i=0}^N$  and  $\{\mathcal{M}^{n,i,t}\}_{i=0}^N$ ;
- 9: **if**  $t > 0$  **then**
- 10:     $\alpha \leftarrow 1/(t+1)$ ;
- 11:     $\mathcal{M}_{\text{reduce}}^{n,t} \leftarrow$  Compute by Equation (16) with  $\bar{\mathcal{M}}_{\text{reduce}}^{n,t}$ ,  $\mathcal{M}'^{n,t-1}$  and  $\alpha$ ;
- 12:   **else**
- 13:      $\mathcal{M}_{\text{reduce}}^{n,t} \leftarrow \bar{\mathcal{M}}_{\text{reduce}}^{n,t}$ ;
- 14:   **end if**
- 15: **return**  $\mathcal{M}_{\text{reduce}}^{n,t}$

---

compute the  $\bar{\mathcal{M}}_{\text{reduce}}^{n,t}$  as:

$$\bar{\mathcal{M}}_{\text{reduce}}^{n,t} = \sum_{i=0}^{\|\mathcal{D}_n^{\text{train}}\|} w_{i,t} \mathcal{M}^{n,i,t} / \sum_{i=0}^{\|\mathcal{D}_n^{\text{train}}\|} w_{i,t}, \quad (14)$$

where the dynamic weight  $w_{i,t}$  is computed as:

$$w_{i,t} = \begin{cases} 1, & \text{if } t = 0 \\ \|\mathcal{M}^{n,i,t} - \mathcal{M}'^{n,t-1}\|_2, & \text{otherwise.} \end{cases} \quad (15)$$

Here, the dynamic weight  $w_{i,t}$  is influenced by the distance between the reduced memory representation  $\mathcal{M}^{n,i,t}$  and the previous memory bank  $\mathcal{M}'^{n,t-1}$ .

After computing  $\bar{\mathcal{M}}_{\text{reduce}}^{n,t}$ , a round-based EMA (rEMA) method is employed to update the memory bank. This approach ensures smoother and more stable updates during the training process. The update rule is defined as:

$$\mathcal{M}_{\text{reduce}}^{n,t} = \alpha \bar{\mathcal{M}}_{\text{reduce}}^{n,t} + (1 - \alpha) \mathcal{M}'^{n,t-1}, \quad (16)$$

where  $\alpha$  represents the exponential decay rate, dynamically calculated as  $\alpha = 1/(t+1)$ . The Memory-reduce is detailed in Algorithm 2.

---

**Algorithm 3** Aggregation on Server  $\mathcal{S}$  for Round  $t$ .

---

**Input:**  $t, \{\mathcal{M}_{\text{reduce}}^{n,t}\}_{n=0}^N$ .

**Output:**  $\bar{\mathcal{M}}^t$ .

- 1:  $m \leftarrow []$ ;
- 2:  $H, W, C \leftarrow \mathcal{M}_{\text{reduce}}^{n,t}.size()$ ;
- 3:  $K \leftarrow HW$ ;
- 4: **for**  $n = 0$  to  $N$  **do**
- 5:    $\{m_{(h,w)}^n\}_{(h=0,w=0)}^{(H,W)} \leftarrow f_{\text{resize}}(\mathcal{M}_{\text{reduce}}^{n,t}, (H, W, C))$ ;
- 6:    $m \leftarrow m \cup \{m_{(h,w)}^n\}_{(h=0,w=0)}^{(H,W)}$ ;
- 7: **end for**
- 8:  $\{c_k \in \mathbb{R}^C\}_{k=0}^K \leftarrow K\text{-means}(m)$ ;
- 9:  $\bar{\mathcal{M}}^t \leftarrow f_{\text{resize}}(\{c_k\}_{k=0}^K, (H, W, C))$ ;
- 10: **return**  $\bar{\mathcal{M}}^t$

---

#### 4.5 $\bar{\mathcal{M}}^t \xleftarrow{\text{agg}} \{\mathcal{M}_{\text{reduce}}^{n,t}\}_{n=0}^N$ on Server

At round  $t$ , the server  $\mathcal{S}$  collects the newly generated memory banks from  $N$  clients, denoted as  $\{\mathcal{M}_{\text{reduce}}^{n,t}\}_{n=0}^N \in \mathbb{R}^{N \times H \times W \times C}$ . The objective of the server is to aggregate these memory banks into a unified, representative memory bank  $\bar{\mathcal{M}}^t$ . This process is formalized as  $\mathcal{S}(\cdot, \cdot): \mathbb{R}^{N \times H \times W \times C} \rightarrow \mathbb{R}^{H \times W \times C}$ . Representation-based federated learning approaches, such as those proposed in (Tan et al. (2022a,b)), utilize weighted aggregation of class prototypes during model updates. However, significant feature bias in the early training stages leads to aggregated memory that deviates significantly from the client-specific memory, which often contains incomplete product types. This misalignment hinders convergence, posing a challenge for clients with limited data diversity. Thus, we employ a clustering-based approach to aggregate the collected memory banks effectively. Specifically, the memory features are represented as  $N \times H \times W$  patch features, denoted by  $m_{(h,w)}^n \in \mathbb{R}^C$ . These patch features are subsequently clustered using the  $K$ -means algorithm, where the number of clusters,  $K$ , corresponds to  $H \times W$ . The clustering results indicate the overall distribution and similarity relationships between the patch-level features stored across all banks at the current stage of the process. Cluster centers describe the representative features of a memory bank. Let  $c_k \in \mathbb{R}^C$  denote the center of the  $k$ -th cluster, serving as a global memory bank updated by  $\bar{\mathcal{M}}^t = f_{\text{resize}}(\{c_k\}_{k=0}^K, (H, W, C))$  and shared

---

**Algorithm 4** Initialization at Round 0.

---

**Input:**  $\{\mathcal{D}_n^{train}\}_{n=0}^N$ ,  $\mathcal{F}(\cdot)$ ,  $\mathcal{P}^n(\cdot, \mathbf{W}^P)$ ,  $\mathcal{G}^n(\cdot, \mathbf{W}^G; \mathbf{G})$ .

**Output:**  $\{\mathcal{M}'^{n,0}\}_{n=0}^N$

- 1: **for** each client  $n$  **in parallel do**
- 2:   Initialize  $\mathbf{W}^P$ ,  $\mathbf{W}^G$  randomly for  $\mathcal{P}^n(\cdot, \mathbf{W}^P)$ ,  $\mathcal{G}^n(\cdot, \mathbf{W}^G; \mathbf{G})$ ;
- 3:   Initialize  $\mathbf{G}$  by Xavier normal initialization for  $\mathcal{G}^n(\cdot, \mathbf{W}^G; \mathbf{G})$ ;
- 4:   **for**  $i = 0$  to  $|\mathcal{D}_n^{train}|$  **do**
- 5:      $\mathcal{M}^i \leftarrow$  Compute by Algorithm 1 with  $t = 0, n, x_i^n, \mathcal{F}(\cdot), \mathbf{W}^P, \mathbf{W}^G, \mathbf{G}$ ;
- 6:   **end for**
- 7:    $\{\mathcal{M}^{n,i,0}\}_{i=0}^{|\mathcal{D}_n^{train}|} \leftarrow [\mathcal{M}^0, \mathcal{M}^1, \dots]$ ;
- 8:    $\mathcal{M}_{reduce}^{n,0} \leftarrow$  Compute by Algorithm 2 with  $n, t = 0$  and  $\{\mathcal{M}^{n,i,0}\}_{i=0}^{|\mathcal{D}_n^{train}|}$ ;
- 9:    $\mathbf{W}^{P,n,0} \leftarrow \mathbf{W}^P$ ,  $\mathbf{W}^{G,n,0} \leftarrow \mathbf{W}^G$ ,  $\mathbf{G}^{n,0} \leftarrow \mathbf{G}$
- 10: **end for**
- 11:  $\{\mathcal{M}_{reduce}^{n,0}\}_{n=0}^N \leftarrow [\mathcal{M}_{reduce}^{0,0}, \mathcal{M}_{reduce}^{1,0}, \dots]$ ;
- 12:  $\bar{\mathcal{M}}^0 \leftarrow$  Compute by Algorithm 3 with  $t = 0$  and  $\{\mathcal{M}_{reduce}^{n,0}\}_{n=0}^N$ ;
- 13: **for**  $n = 0$  to  $N$  **do**
- 14:    $\mathcal{M}'^{n,0} \leftarrow \bar{\mathcal{M}}^0$ ;
- 15: **end for**
- 16: **return**  $\{\mathcal{M}'^{n,0}\}_{n=0}^N \leftarrow [\mathcal{M}'^{0,0}, \mathcal{M}'^{1,0}, \dots]$

---

across individual clients,  $\forall n \in N$ ,  $\mathcal{M}'^{n,t} = \bar{\mathcal{M}}^t$ . The aggregation methodology is outlined in Algorithm 3, while the comprehensive training procedure for FedDyMem is presented in Algorithm 5.

## 4.6 Testing for Anomaly Detection on Clients

During the testing phase, as shown in Fig. 2(b), each client employs the globally aggregated memory bank  $\bar{\mathcal{M}}^T$ , received from the server at the end of training, to perform anomaly detection on its local test samples. Following prior works (Roth et al. (2022); Lee et al. (2022)), we utilize a nearest neighbor search in the feature space to calculate the anomaly score for each test sample  $x^{test} \in \mathcal{D}^{test}$ .

Given a test image  $x^{test}$  on  $n$ -th client, the well trained local models  $\mathbf{W}^{P,n,T}$ ,  $\mathbf{W}^{G,n,T}$  and  $\mathbf{G}^{n,T}$  are used to extract the memory feature representation  $\mathcal{M}^{test} \in \mathbb{R}^{H \times W \times C}$  following the same

---

**Algorithm 5** Training for FedDyMem.

---

**Input:**  $N$  Clients  $\{\mathcal{C}_n\}_{n=1}^N$  with  $\{\mathcal{D}_n^{train}\}_{n=0}^N$ , one server  $\mathcal{S}$ , the number of rounds  $T$ , the local epochs  $E$ .

- 1:  $\{\mathcal{M}'^{n,0}\}_{n=0}^N \leftarrow$  Initialization by Algorithm 4;
- 2: **for**  $t = 1$  to  $T$  **do**
- 3:   **for** each client  $n$  **in parallel do**
- 4:      $\mathcal{M}_{reduce}^{n,t} \leftarrow ClientUpdate(n, t, E, \mathcal{D}_n^{train})$ ;
- 5:   **end for**
- 6:    $\{\mathcal{M}_{reduce}^{n,t}\}_{n=0}^N \leftarrow$  Collection all memory bank from  $N$  clients;
- 7:    $\bar{\mathcal{M}}^t \leftarrow$  Upload  $\{\mathcal{M}_{reduce}^{n,t}\}_{n=0}^N$  to  $\mathcal{S}$  and computed by Algorithm 3;
- 8: **end for**
- 9: Save all well trained  $\{\mathbf{W}^{P,n,T}, \mathbf{W}^{G,n,T}, \mathbf{G}^{n,T}\}_{n=0}^N$  and  $\bar{\mathcal{M}}^T$  locally.
- 10:  $ClientUpdate(n, t, E, \mathcal{D}_n^{train})$ :
- 11:   **for**  $e = 0$  to  $E$  **do**
- 12:     **for**  $i = 0$  to  $|\mathcal{D}_n^{train}|$  **do**
- 13:        $\mathcal{M}^i \leftarrow$  Compute by Algorithm 1 with  $t, n, x_i^n$ ;
- 14:        $\ell \leftarrow$  Compute loss by Equation (12) with  $\mathcal{M}^i$  and  $\mathcal{M}'^{n,t-1}$ ;
- 15:       Update  $\{\mathbf{W}^{P,n,t}, \mathbf{W}^{G,n,t}, \mathbf{G}^{n,t}\}$  by  $\ell$  and Adam Optimizer;
- 16:     **end for**
- 17:   **end for**
- 18:    $\{\mathcal{M}^{n,i,t}\}_{i=0}^{|\mathcal{D}_n^{train}|} \leftarrow$  Compute  $[\mathcal{M}^0, \mathcal{M}^1, \dots]$  by trained  $\{\mathbf{W}^{P,n,t}, \mathbf{W}^{G,n,t}, \mathbf{G}^{n,t}\}$ ;
- 19:    $\mathcal{M}_{reduce}^{n,t} \leftarrow$  Compute by Algorithm 2 with  $n, t$  and  $\{\mathcal{M}^{n,i,t}\}_{i=0}^{|\mathcal{D}_n^{train}|}$ ;
- 20: **return**  $\mathcal{M}_{reduce}^{n,t}$

---

procedure as in training. For each spatial location  $(h, w)$ , the corresponding feature patch  $m_{(h,w)}^{test} \in \mathbb{R}^C$  is compared with the final global memory bank  $\bar{\mathcal{M}}^T = \{\bar{m}_d \in \mathbb{R}^C\}_{d=1}^{H \times W}$  to compute its anomaly score. The pixel-wise anomaly score  $a_{(h,w)}$  is computed as the minimum Euclidean distance to its  $K$  nearest neighbors in the memory bank. And the image-level anomaly score  $\mathcal{A}^{test}$  is computed by the softmax-weighted maximum strategy:

$$\mathcal{A}^{test} = \max_{(h,w)} \left( a_{(h,w)} \cdot \frac{\exp(a_{(h,w)})}{\sum_{h',w'} \exp(a_{(h',w')})} \right). \quad (17)$$

## 4.7 Privacy Analysis

In federated learning, Mutual Information(MI) is a fundamental tool for evaluating privacy. Prior studies (Zhang et al. (2023); Alsulaimawi (2024); Ji et al. (2025); Tan et al. (2024)) indicate that MI provides a principled paradigm for privacy analysis and can jointly improve privacy and utility. Consistent with prior work, we adopt a MI-based methodology to analyze FedDyMem’s privacy. For two statistics  $X$  and  $Y$ , their mutual information  $I(X; Y)$  quantifies statistical dependence; under Gaussian assumptions,

$$I(X; Y) = -\frac{1}{2} \log(1 - \rho_{xy}^2). \quad (18)$$

where  $\rho_{xy}$  denotes the Pearson correlation coefficient. A smaller  $I(X; Y)$  implies that an adversary can extract less information about  $X$  from observing  $Y$ , indicating stronger privacy.

In our FedDyMem, let  $x^j$  be a raw sample,  $\mathcal{M}^j = f(x^j)$  denotes its corresponding memory feature. The reduced memory  $\mathcal{M}_{reduce} \leftarrow [\mathcal{M}^0, \mathcal{M}^1, \dots]$  is obtained via weighted averaging and the rEMA update, which induces the Markov chain  $x^j \rightarrow (\mathcal{M}^0, \mathcal{M}^1, \dots) \rightarrow \mathcal{M}_{reduce}$ . By the data-processing inequality (DPI), the mutual information decreases after memory-reduce, i.e.,

$$I(x^j; \mathcal{M}_{reduce}) \leq I(x^j; \mathcal{M}^j), \quad (19)$$

which qualitatively captures the privacy effect of the memory-reduce module. Building on this Lemma 1 together with Theorem 1 provides a more rigorous and quantitative formulation of this privacy-preserving capability.

**Lemma 1** (Correlation Quantitative Bound) *Let  $\{Y_i\}_{i=1}^N$  be scalar statistics and define the normalized weighted average  $Y = \sum_{i=1}^N \tilde{w}_i Y_i$  with  $\tilde{w}_i \geq 0$ ,  $\sum_i \tilde{w}_i = 1$ . Assume:*

1.  $X_j$  is independent of  $Y_i$  for  $i \neq j$ .
2. Each  $Y_i$  has finite, strictly positive variance  $\sigma_{Y_i}^2$ , and  $\text{Cov}(Y_i, Y_k) \geq 0$  for  $i \neq k$ .

Denote  $\sigma_{Y_i}^2 = \text{Var}(Y_i)$ , then

$$|\rho(X_j, Y)| \leq \frac{\tilde{w}_j \sigma_{Y_j}}{\sqrt{\sum_{i=1}^N \tilde{w}_i^2 \sigma_{Y_i}^2}} |\rho(X_j, Y_j)|. \quad (20)$$

*Proof* By linearity and independence,  $\text{Cov}(X_j, Y) = \tilde{w}_j \text{Cov}(X_j, Y_j)$ , hence

$$|\rho(X_j, Y)| = \frac{|\text{Cov}(X_j, Y)|}{\sigma_{X_j} \sigma_Y} = \frac{\tilde{w}_j |\text{Cov}(X_j, Y_j)|}{\sigma_{X_j} \sigma_Y}. \quad (21)$$

For the denominator,

$$\text{Var}(Y) = \sum_{i=1}^N \tilde{w}_i^2 \sigma_{Y_i}^2 + 2 \sum_{1 \leq i < k \leq N} \tilde{w}_i \tilde{w}_k \text{Cov}(Y_i, Y_k). \quad (22)$$

Since  $\text{Cov}(Y_i, Y_k) \geq 0$ , with  $\sigma_Y = \sqrt{\text{Var}(Y)}$ , the variance satisfies  $\sigma_Y = \sqrt{\text{Var}(Y)} \geq \sqrt{\sum_{i=1}^N \tilde{w}_i^2 \sigma_{Y_i}^2}$ .

Substituting this bound into the denominator of (21) with  $|\text{Cov}(X_j, Y_j)| = \sigma_{X_j} \sigma_{Y_j} |\rho(X_j, Y_j)|$ , completes the proof.  $\square$

**Theorem 1** (Memory-Reduce Privacy) *For any client sample  $x^j$  with memory feature  $\mathcal{M}^j$  and reduced memory  $\mathcal{M}_{reduce}$ ,*

$$I(x^j; \mathcal{M}_{reduce}) \ll I(x^j; \mathcal{M}^j). \quad (23)$$

*Proof* Following (14)(16) we define  $x^j$  as  $X_j$  and  $\mathcal{M}_{reduce}$  as the normalized weighted average  $Y$  in Lemma 1. Thus, the correlation between  $x^j$  and the reduced memory satisfies

$$|\rho(x^j, \mathcal{M}_{reduce})| \leq \frac{\tilde{w}_j \sigma_{\mathcal{M}^j}}{\sqrt{\sum_{i=1}^{|D|} \tilde{w}_i^2 \sigma_{\mathcal{M}^j}^2}} |\rho(x^j, \mathcal{M}^j)|, \quad (24)$$

where  $|D|$  denotes the number of local samples at the client.

Since mutual information is monotone in  $|\rho|$ , we obtain

$$\frac{I(x^j; \mathcal{M}_{reduce})}{I(x^j; \mathcal{M}^j)} \leq \frac{-\frac{1}{2} \log \left( 1 - \frac{\tilde{w}_j^2 \sigma_{\mathcal{M}^j}^2}{\sum_{i=1}^{|D|} \tilde{w}_i^2 \sigma_{\mathcal{M}^j}^2} \rho(x^j, \mathcal{M}^j)^2 \right)}{-\frac{1}{2} \log(1 - \rho(x^j, \mathcal{M}^j)^2)}. \quad (25)$$

Moreover, since the averaging denominator grows with the number of samples  $|D|$ , the effective scaling factor

$$\frac{\tilde{w}_j^2 \sigma_{\mathcal{M}^j}^2}{\sum_{i=1}^{|D|} \tilde{w}_i^2 \sigma_{\mathcal{M}^j}^2} \ll 1, \quad (26)$$

which proves the Theorem 1.  $\square$

By (26), the per-sample scaling vanishes as  $|D|$  grows. Under the bounded-variance conditions in Lemma 1, this yields  $|\rho(x^j, \mathcal{M}_{reduce})| \rightarrow 0$  and therefore  $I(x^j; \mathcal{M}_{reduce})$  as  $|D| \rightarrow \infty$ , making the per-sample leakage asymptotically negligible. This establishes that the privacy leakage diminishes both with more samples, providing a

strong quantitative guarantee, confirming that the proposed memory-reduce is essential for privacy preservation. Furthermore, FedDyMem exchanges statistical summaries (memory banks) rather than model parameters (Tan et al. (2022a)) and the transmitted memory features are derived from multi-layer, low-dimensional representations via irreversible mappings (Li et al. (2023b)).

## 5 Convergence Analysis

We analyze the convergence of FedDyMem under a non-convex loss. Let the loss at local iteration  $e$  in communication round  $t$  be  $\mathcal{L}_{t,e} := \mathbb{E}_{x \sim \mathcal{D}_n}[\ell(\mathcal{M}^{t,e}, \mathcal{M}'^{t-1})]$ , where  $\mathcal{M}^{t,e} = f(x; \theta_{t,e})$  and its Jacobian as  $J_f(x; \theta_{t,e})$ . Here  $\mathcal{M}'^{t-1}$  is the center memory received at round  $t$ . Some common assumptions based on existing frameworks are reasonably presented below.

**Assumption 1** ( $L_M$ -smooth) *Within a fixed communication round  $t$ , treat  $\mathcal{M}'^{t-1}$  as a constant. Excluding the measure-zero non-differentiable set,*

$$\|\nabla_{\mathcal{M}} \ell(\mathcal{M}, \mathcal{M}') - \nabla_{\mathcal{M}} \ell(\tilde{\mathcal{M}}, \mathcal{M}')\|_2 \leq L_M \|\mathcal{M} - \tilde{\mathcal{M}}\|_2, \quad (27)$$

and  $\|\nabla_{\mathcal{M}} \ell(\mathcal{M}, \mathcal{M}')\|_2 \leq G_M$ . By the chain rule, the composite smoothness constant satisfies  $L_\theta \leq B_J^2 L_M$ , and  $\|\nabla_\theta \ell(\mathcal{M}, \mathcal{M}')\|_2 \leq B_J G_M$ .

**Assumption 2** (Bounded features and Jacobian) *There exist constants  $R_M, B_J > 0$  such that, for any  $\theta, x$ , satisfies  $\|f(x; \theta)\|_2 \leq R_M$ ,  $\|J_f(x; \theta)\|_2 \leq B_J$ .*

**Assumption 3** (Unbiased stochastic gradients with bounded variance) *The local SGD gradient estimate  $g_{t,e}$  satisfies*

$$\mathbb{E}[g_{t,e}] = \nabla_\theta \mathbb{E}_{x \sim \mathcal{D}_n}[\ell(\mathcal{M}^{t,e}, \mathcal{M}'^{t-1})], \quad (28)$$

and  $\mathbb{E}\|g_{t,e} - \nabla_\theta \mathbb{E}_x[\ell(\mathcal{M}^{t,e}, \mathcal{M}'^{t-1})]\|_2^2 \leq \sigma^2$ .

**Assumption 4** (Lipschitz Continuity in  $\mathcal{M}'$ ) *Client-side reduction and server aggregation are convex combinations. Together with Assumption 2, this implies  $\|\mathcal{M}'^t\|_2 \leq R_M$ , hence  $\text{dis}(m_{(h,w)}, m'_k) \leq 2R_M$  and  $0 \leq \ell(\cdot, \cdot) \leq 2R_M$ . Moreover, the map  $\ell(\mathcal{M}, \cdot)$  is 1-Lipschitz in  $\mathcal{M}'$ :*

$$|\ell(\mathcal{M}, \mathcal{M}') - \ell(\mathcal{M}, \tilde{\mathcal{M}}')| \leq \|\mathcal{M}' - \tilde{\mathcal{M}}'\|_2. \quad (29)$$

This follows from the bounded convex hull, max-hinge, and the triangle inequality.

**Theorem 2** (Round Loss Reduction) *Within a fixed communication round  $t$ , under Assumptions 1–4, for any client and local iterations  $e = 0, \dots, E-1$ , if  $\eta \in (0, 2/L_\theta)$ , then*

$$\begin{aligned} \mathbb{E}[\mathcal{L}_{t,E}] &\leq \mathbb{E}[\mathcal{L}_{t,0}] - \left(\eta - \frac{\eta^2 L_\theta}{2}\right) \sum_{e=0}^{E-1} \mathbb{E}\left[\|\nabla_\theta \mathcal{L}_{t,e}\|_2^2\right] \\ &\quad + \frac{E \eta^2 L_\theta}{2} \sigma^2, \end{aligned} \quad (30)$$

and  $\forall e$ ,  $\mathbb{E}[\mathcal{L}_{t,e}] \leq 2R_M < \infty$ .

*Proof* Assumption 4 implies  $\text{dis}(m, m') \leq 2R_M$ , hence  $\max(0, \text{dis} - th) \leq \max(0, 2R_M - th) \leq 2R_M$ , as  $th > 0$ . Therefore  $\mathbb{E}[\mathcal{L}_{t,e}] \leq 2R_M$ .

Let the update be  $\theta_{t,e+1} = \theta_{t,e} - \eta g_{t,e}$ . By the Assumption 1, apply the one-step smooth upper bound to  $\theta \mapsto \mathbb{E}[\mathcal{L}_{t,e}]$ :

$$\begin{aligned} \mathbb{E}[\mathcal{L}_{t,e+1}] &\leq \mathbb{E}[\mathcal{L}_{t,e}] + \langle \nabla_\theta \mathbb{E}[\mathcal{L}_{t,e}], \theta_{t,e+1} - \theta_{t,e} \rangle \\ &\quad + \frac{L_\theta}{2} \|\theta_{t,e+1} - \theta_{t,e}\|_2^2 \\ &\leq \mathbb{E}[\mathcal{L}_{t,e}] - \eta \mathbb{E}[\langle \nabla_\theta \mathcal{L}_{t,e}, g_{t,e} \rangle] + \frac{\eta^2 L_\theta}{2} \mathbb{E}\|g_{t,e}\|_2^2. \end{aligned}$$

By Assumption 3,  $\mathbb{E}[g_{t,e}] = \mathbb{E}[\nabla_\theta \mathcal{L}_{t,e}]$  and  $\mathbb{E}\|g_{t,e}\|_2^2 = \mathbb{E}\|\nabla_\theta \mathcal{L}_{t,e}\|_2^2 + \sigma^2$ ; substituting yields

$$\mathbb{E}[\mathcal{L}_{t,e+1}] \leq \mathbb{E}[\mathcal{L}_{t,e}] - \left(\eta - \frac{\eta^2 L_\theta}{2}\right) \mathbb{E}\|\nabla_\theta \mathcal{L}_{t,e}\|_2^2 + \frac{\eta^2 L_\theta}{2} \sigma^2.$$

Summing over  $e = 0, \dots, E-1$  gives (30).  $\square$

**Theorem 3** (FedDyMem Convergence) *Under Assumptions 1–4 with fixed local steps  $E \geq 1$ , as  $T \rightarrow \infty$ , we have*

$$\frac{1}{TE} \sum_{t=1}^T \sum_{e=0}^{E-1} \mathbb{E}\left[\|\nabla_\theta \mathcal{L}_{t,e}\|_2^2\right] \rightarrow 0. \quad (31)$$

*Proof* Sum Theorem 2 over  $t = 1, \dots, T$  to obtain

$$\begin{aligned} &\left(\eta - \frac{\eta^2 L_\theta}{2}\right) \sum_{t=1}^T \sum_{e=0}^{E-1} \mathbb{E}\|\nabla_\theta \mathcal{L}_{t,e}\|_2^2 \\ &\leq \sum_{t=1}^T (\mathbb{E}[\mathcal{L}_{t,0}] - \mathbb{E}[\mathcal{L}_{t,E}]) + T \cdot \frac{E \eta^2 L_\theta}{2} \sigma^2. \end{aligned} \quad (32)$$

Apply a decomposition to the first term on the right:

$$\begin{aligned} \sum_{t=1}^T (\mathbb{E}[\mathcal{L}_{t,0}] - \mathbb{E}[\mathcal{L}_{t,E}]) &= \mathbb{E}[\mathcal{L}_{1,0}] - \mathbb{E}[\mathcal{L}_{T,E}] \\ &\quad + \sum_{t=1}^{T-1} (\mathbb{E}[\mathcal{L}_{t+1,0}] - \mathbb{E}[\mathcal{L}_{t,E}]), \end{aligned} \quad (33)$$

Let  $\Delta_t := \mathbb{E}\|\mathcal{M}'^t - \mathcal{M}'^{t-1}\|_2$ . By the 1-Lipschitz property in Assumption 4,

$$\mathbb{E}[\mathcal{L}_{t+1,0}] - \mathbb{E}[\mathcal{L}_{t,E}] \leq \Delta_t. \quad (34)$$

Using the lower bound  $\mathbb{E}[\mathcal{L}_{T,E}] \geq \underline{\ell}$ , substitute back into (32) and divide both sides by  $TE(\eta - \eta^2 L_\theta/2)$  to get

$$\begin{aligned} \frac{1}{TE} \sum_{t=1}^T \sum_{e=0}^{E-1} \mathbb{E} \left[ \|\nabla_\theta \mathcal{L}_{t,e}\|_2^2 \right] &\leq \frac{\mathbb{E}[\mathcal{L}_{1,0}] - \underline{\ell}}{(\eta - \eta^2 L_\theta/2) TE} \\ &+ \frac{\eta L_\theta}{2(\eta - \eta^2 L_\theta/2)} \sigma^2 + \frac{1}{(\eta - \eta^2 L_\theta/2) TE} \sum_{t=1}^{T-1} \Delta_t. \end{aligned} \quad (35)$$

For the first term, with  $\eta \in (0, 2/L_\theta)$  and  $E \geq 1$ , the numerator is constant while the denominator grows linearly in  $T$ , hence it vanishes. For the second term, either use decreasing step sizes, leading to a noise factor proportional to  $(\sum_{t,e} \eta_{t,e}^2) / (\sum_{t,e} \eta_{t,e}) \rightarrow 0$  if  $\sum \eta_{t,e} = \infty$  and  $\sum \eta_{t,e}^2 < \infty$ , or fix  $\eta$  and increase batch size so that  $\sigma^2 \rightarrow 0$ ; in both cases the term vanishes. For the third term, using (16) and Assumption 4, we have

$$\Delta_t = \alpha_t \mathbb{E} \|\widehat{\mathcal{M}}'^t - \mathcal{M}'^{t-1}\| \leq \frac{2R_M}{t+1}.$$

Thus  $\sum_{t=1}^{T-1} \Delta_t = O(\log T)$ , and after normalization by  $TE$  it tends to 0. Combining the three parts proves the claim.  $\square$

The above analysis shows that the expected loss-gradient converges to zero as iterations increase, thereby proving FedDyMem's convergence.

## 6 Experiments

All experiments presented in this article were implemented and conducted using the PyTorch framework. Model training was performed on a high-performance computing system equipped with AMD EPYC 9554 64-core processors and eight NVIDIA GeForce RTX A6000 GPUs, each possessing 48 GB of memory, to ensure accelerated computation.

### 6.1 Experimental Settings

**Datasets.** In this article, we combined 6 image anomaly detection datasets containing different types of data, covering various industrial inspection scenarios and medical imaging domains, to evaluate the performance of FedDyMem. These datasets are as follows:

- **Mixed-Brain-AD(Brain):** We combined 3 brain image diagnostic datasets, including Brain-Tumor (Cai et al. (2024)), BraTS2021 (Baid et al. (2021)) and HeadCT (Salehi et al. (2021)). These datasets, consisting of both MRI and CT images, were distributed across different clients in a heterogeneous manner to represent a mixture of various image types.
- **Mixed-ChestXray-AD(X-ray):** Three diagnostic chest X-ray datasets, including ChestXRay2017 (Kermany et al. (2018)), RSNA (Wang et al. (2017)), and VinDr-CXR (Nguyen et al. (2022)), were employed in this article. These datasets were derived from distinct medical institutions, ensuring a diverse and heterogeneous data distribution, which is essential for the federated UAD.
- **Mixed-PCB-AD(PCB):** We investigate 2 datasets containing PCB anomalies, namely VisA (Zou et al. (2022)) and VISION (Bai et al. (2023)), and integrate them to create the Mixed-PCB dataset. The VisA dataset includes six different types of PCB products, while the VISION dataset encompasses two types. Consequently, the Mixed-PCB-AD dataset provides a total of 8 distinct types of PCB product images, facilitating simulation in federated UAD.
- **MVTec (Bergmann et al. (2019)):** In this article, we utilize 5 texture classes(carpet, grid, leather, tile, and wood) from the MVTec dataset, which includes mask annotations, to simulate industrial federated anomaly detection scenarios.
- **MetalPartsAD(MPDD) (Jezek et al. (2021)):** The MPDD comprises images of 6 types of metal parts, each captured under varying conditions of spatial orientation, object positioning, and camera distance. These images are further characterized by diverse lighting intensities and non-homogeneous backgrounds, providing a comprehensive dataset for our federated UAD.
- **TextureAD-Wafer(Wafer) (Lei et al. (2025)):** TextureAD-Wafer comprises a dataset of 14 distinct wafer products, each imaged using an industrial-grade, high-resolution optical camera. This dataset also explores these wafer products under various optical conditions, thus providing a rich federated UAD simulate environment with diverse feature distributions.

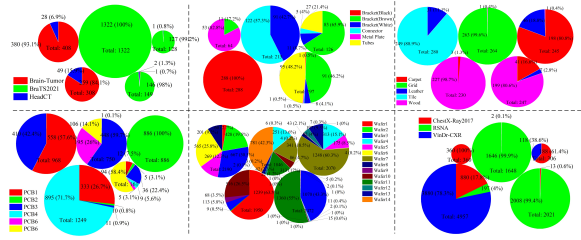


**Fig. 5** Summary of the dataset distribution on five clients. The relative sizes of the pie in the chart illustrate the total data volume across individual clients. Distinct colors within each pie represent different product types.

**Scenes with Feature Distribution Bias.** In this article, we aim to simulate heterogeneous feature distributions across 5 clients by using all samples from the same normal categories with different product types. We employ a Dirichlet distribution to allocate data, where each product type, though labeled as normal, is distributed to various clients. We set the Dirichlet parameter  $\alpha = 0.1$  to accentuate the variances in data distribution across clients, thus simulating more realistic and challenging multi-client scenarios typically encountered in federated UAD. Fig. 5 illustrates the results of this partitioning approach across all datasets.

**Implementation Details.** The frozen feature extractor used in our experiments is the Wide-ResNet-50 model pre-trained on the ImageNet dataset. For FedDyMem, the hyperparameters  $H^G$  and  $W^G$  are set to 8, and  $th$  is set to 0.01. All baseline models are constructed using the Wide-ResNet-50, with all parameters comprehensively aggregated. The parameter  $K$  for the KNN algorithm is set to 3. For a fair comparison with other state-of-the-art methods, we ensure consistency in the training parameters used in our experiments. Specifically, the learning rate is set to  $1 \times 10^{-3}$ , with a total of 200 communication rounds. The local epoch is set to 1, and the batch size is 10. We utilize the Adam optimizer with a weight decay of  $5 \times 10^{-4}$  and a momentum of 1. All images in the dataset were preprocessed by cropping and resizing to a resolution of  $224 \times 224$  pixels using the bicubic interpolation method.

**Evaluation Metric.** For the evaluation of anomaly detection, we adopt the Area Under the Receiver Operating Characteristic Curve

(AUROC), ensuring a comprehensive assessment of our proposed model in alignment with prior studies. Image-level anomaly detection performance is quantified using the standard AUROC metric, denoted as Image-level AUROC(I-AUROC). Additionally, to assess anomaly localization, we compute the Pixel-level AUROC(P-AUROC). To further enhance the evaluation of anomaly localization capabilities, we calculate the Per-Region Overlap (PRO) at the pixel level, providing a more granular and comprehensive analysis. These metrics are widely used in previous work (Roth et al. (2022); You et al. (2022); Liang et al. (2023); Cai et al. (2024)).

## 6.2 Convergence Curves and Distribution Consistency

In this section, we present a detailed analysis of the training loss curves for FedDyMem in comparison with baseline models across four datasets including Brain, Wafer, PCB, and X-ray. The loss curves for all 5 clients are illustrated in Fig. 6 over 200 communication rounds, providing insights into the performance and convergence behavior of the models. First, FedDyMem demonstrates a significantly faster convergence rate across all datasets. Second, FedDyMem exhibits smoother convergence compared to the baseline models. As shown in the zoomed-in view of the later communication rounds in Fig. 6, the loss curves of the baseline models have less stable optimization dynamics. In contrast, FedDyMem maintains consistent and stable convergence. Moreover, FedDyMem consistently achieves lower final loss values across all datasets. The experimental results substantiate the convergence analysis presented in Section 5, further validating the efficiency of FedDyMem in federated learning settings.

To further analyze the discrepancy between the loss values in Fig. 6 and the AUROC improvements reported in Table 1, we visualize in Fig. 7 the t-SNE of the memory feature distributions learned by FedAvg and FedDyMem on the MVTec dataset after 200 communication rounds. Specifically, we compare the local memory banks of five clients against their corresponding global memory banks in Fig. 7(a). For FedAvg, the memory features generated by individual clients exhibit clear distributional deviations from the global memory, leading to local losses that remain several orders

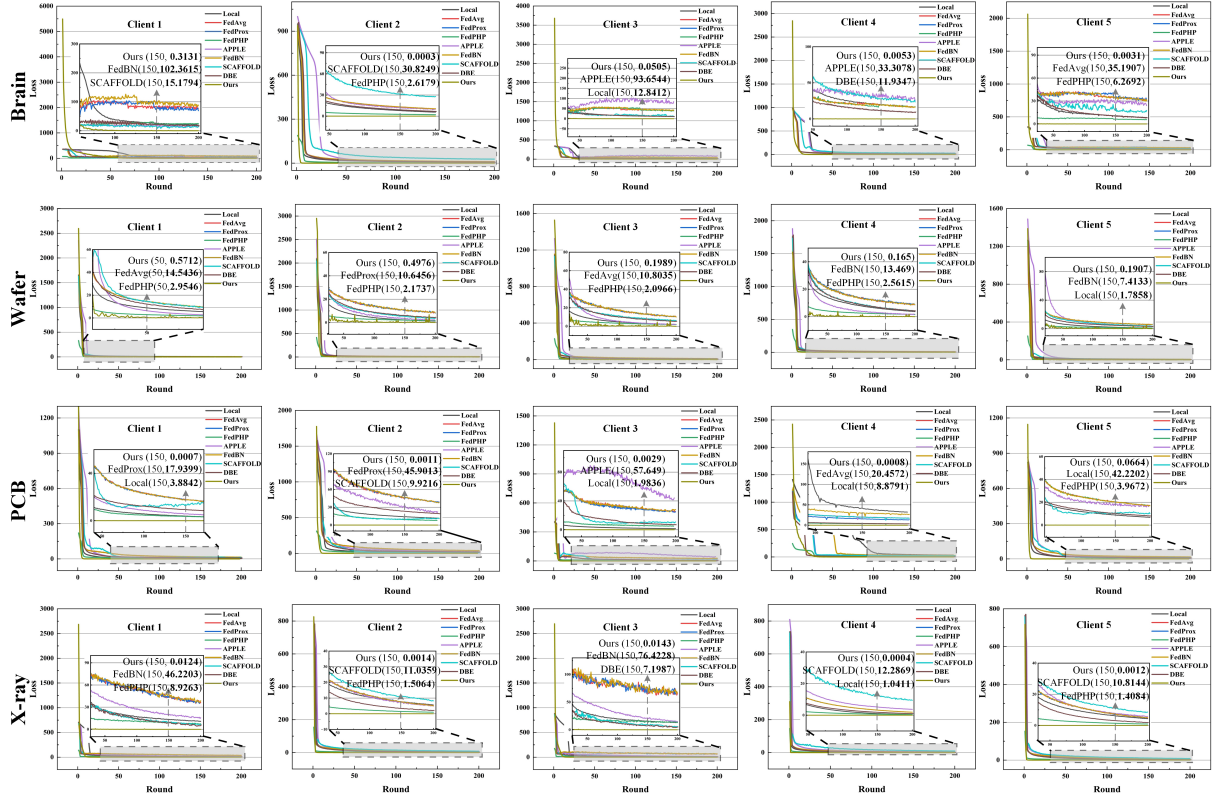


**Fig. 6** Illustration of the loss curves across five clients evaluated on four datasets. To better highlight the effectiveness of FedDyMem, zoom-in views of the later communication rounds are included in each subplot. In the zoom-in, we annotate three key values: (1) the loss of FedDyMem (Ours) as the first row, (2) the maximum loss among all compared methods in the second row, and (3) the minimum loss excluding our method in the third row.

of magnitude higher (up to  $10^4$ ) than those of FedDyMem. This mismatch indicates that although the optimization objective in FedAvg continues to decrease, the learned memory features fail to align with the global feature distribution due to local feature bias and inter-client distribution shifts. Furthermore, Fig. 7(b) illustrates that FedDyMem achieves a much more compact and coherent global feature space across clients. The memory features aggregated via dynamic memory update and k-means clustering form a well-aligned global representation that mitigates the impact of intra-class distribution bias. This alignment is critical for UAD, where the effectiveness of nearest-neighbor-based scoring relies heavily on the quality and consistency of the global memory. Therefore, the superior AUROC performance of FedDyMem benefits from its ability to construct globally consistent and discriminative feature spaces across heterogeneous clients.

### 6.3 Performance Comparisons with Existing Methods

To demonstrate the superior performance of FedDyMem, we conducted extensive comparative analyses with 8 baseline models. These include the basic federated learning algorithm FedAvg (McMahan et al. (2017)), the regularization-based FedProx (Li et al. (2020b)), the personalized-based FedPHP (Li et al. (2021c)) and APPLE (Luo and Wu (2022)). Additionally, we compared against domain-skew-oriented methods such as FedBN (Li et al. (2021b)) and SCAFFOLD (Karimireddy et al. (2020)), as well as the model-splitting method DBE (Zhang et al. (2024b)) and a purely local training scheme (Local).

**Training Process.** Fig. 8 illustrates the I-AUROC performance of the FedDyMem training process in comparison with baseline models on all datasets. FedDyMem achieves superior testing

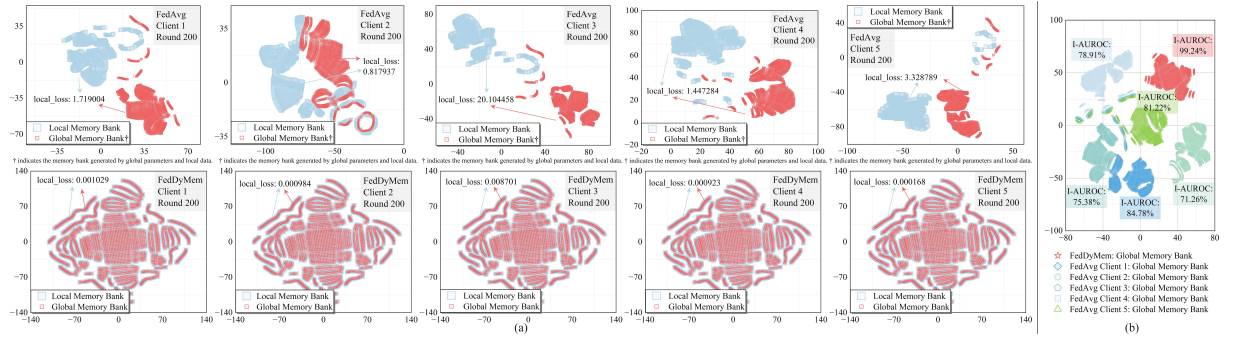


**Fig. 7** Comparison of feature distributions on the MVTec dataset after 200 communication rounds. (a) t-SNE (Maaten and Hinton (2008)) visualization of local and global memory banks generated by five clients using FedAvg (top row) and FedDyMem (bottom row). (b) Comparison of global memory banks aggregated from FedDyMem and FedAvg clients, together with the corresponding I-AUROC results.

**Table 1** Comparison of Image-AUROC (%) results on six Dataset

Methods	Communication	Wafer	PCB	MVTec	MPDD	Brain	X-ray
Local	-	57.35 ( $\pm 0.71$ )	51.89 ( $\pm 0.76$ )	75.94 ( $\pm 0.39$ )	54.39 ( $\pm 0.77$ )	50.66 ( $\pm 0.87$ )	61.02 ( $\pm 0.58$ )
FedAvg		63.91 ( $\pm 0.36$ )	54.18 ( $\pm 0.33$ )	80.32 ( $\pm 0.81$ )	61.87 ( $\pm 0.63$ )	50.16 ( $\pm 0.56$ )	61.48
FedProx	Model Parameters: $\approx 10.66M$ , (SCAFFOLD)	63.98 ( $\pm 0.51$ )	54.11 ( $\pm 0.48$ )	80.22 ( $\pm 0.78$ )	61.83 ( $\pm 0.61$ )	50.47 ( $\pm 0.34$ )	61.45
FedPHP	$\approx 10.66M * 2$	63.94 ( $\pm 0.56$ )	54.13 ( $\pm 0.36$ )	80.19 ( $\pm 0.62$ )	61.80 ( $\pm 0.63$ )	50.38 ( $\pm 0.39$ )	61.45
APPLE		65.92 ( $\pm 0.33$ )	56.79 ( $\pm 0.65$ )	82.43 ( $\pm 0.51$ )	61.03 ( $\pm 0.77$ )	50.82 ( $\pm 0.45$ )	68.47
FedBN		63.89 ( $\pm 0.35$ )	54.09 ( $\pm 0.79$ )	80.13 ( $\pm 0.77$ )	61.90 ( $\pm 0.61$ )	50.04 ( $\pm 0.54$ )	61.45
SCAFFOLD		66.53 ( $\pm 0.85$ )	63.56 ( $\pm 0.30$ )	83.26 ( $\pm 0.37$ )	59.41 ( $\pm 0.80$ )	49.90 ( $\pm 0.52$ )	72.52
DBE		64.12 ( $\pm 0.49$ )	53.78 ( $\pm 0.38$ )	79.78 ( $\pm 0.90$ )	61.78 ( $\pm 0.51$ )	50.06 ( $\pm 0.85$ )	62.77
<b>Ours</b>	Memory Size: $\approx 5.62M$	<b>71.96 (<math>\pm 0.32</math>)</b>	<b>83.34 (<math>\pm 0.45</math>)</b>	<b>99.24 (<math>\pm 0.36</math>)</b>	<b>83.93 (<math>\pm 0.77</math>)</b>	<b>89.27 (<math>\pm 0.45</math>)</b>	<b>80.30 (<math>\pm 0.36</math>)</b>

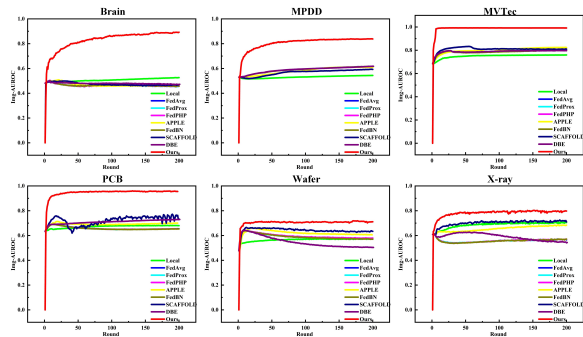


**Fig. 8** Illustration of I-AUROC test accuracy comparing FedDyMem and baseline models.

accuracy compared to other baseline models, while also exhibiting a more stable training process.

Specifically, the baseline models exchange parameters exclusively during communication rounds, introducing a distribution bias for memory features. This limitation prevents the models from achieving suboptimal solutions.

**Communication Cost.** In federated learning, communication efficiency is crucial for practical deployment, especially in bandwidth-constrained or latency-sensitive environments. As shown in Table 1, most existing methods (e.g., FedAvg, FedProx, APPLE) require extensive communication of full model parameters, which amount to approximately 10.66 MB per communication round. In contrast, our approach only requires the exchange of a memory bank of approximately 5.62MB during each communication round. This substantially reduces communication overhead,

**Table 2** Comparison of Pixel-AUROC (%) results on four Dataset

Methods	Wafer	PCB	MVTec	MPDD
Local	58.27( $\pm 1.20$ )	68.12( $\pm 1.11$ )	72.63( $\pm 0.98$ )	87.02( $\pm 1.05$ )
FedAvg	66.56( $\pm 0.70$ )	69.30( $\pm 0.34$ )	76.16( $\pm 0.73$ )	91.67( $\pm 0.94$ )
FedProx	66.41( $\pm 0.74$ )	69.10( $\pm 1.28$ )	76.08( $\pm 1.28$ )	91.59( $\pm 1.02$ )
FedPHP	66.44( $\pm 1.38$ )	69.11( $\pm 0.42$ )	76.03( $\pm 0.57$ )	91.56( $\pm 0.73$ )
APPLE	69.88( $\pm 0.95$ )	71.34( $\pm 0.85$ )	78.06( $\pm 1.08$ )	92.12( $\pm 1.19$ )
FedBN	66.32( $\pm 0.57$ )	68.91( $\pm 0.82$ )	75.92( $\pm 1.34$ )	91.59( $\pm 0.38$ )
SCAFFOLD	68.75( $\pm 1.19$ )	77.18( $\pm 0.54$ )	80.81( $\pm 0.35$ )	93.47( $\pm 0.74$ )
DBE	66.95( $\pm 1.07$ )	72.95( $\pm 1.35$ )	76.18( $\pm 0.89$ )	92.66( $\pm 1.36$ )
<b>Ours</b>	<b>78.40(<math>\pm 1.31</math>)</b>	<b>96.03(<math>\pm 0.79</math>)</b>	<b>97.04(<math>\pm 0.56</math>)</b>	<b>98.97(<math>\pm 1.39</math>)</b>

**Table 3** Comparison of PRO (%) results on four Dataset

Methods	Wafer	PCB	MVTec	MPDD
Local	47.76( $\pm 0.52$ )	45.86( $\pm 1.31$ )	56.97( $\pm 0.48$ )	51.31( $\pm 0.73$ )
FedAvg	67.00( $\pm 0.30$ )	54.04( $\pm 0.57$ )	53.35( $\pm 1.49$ )	55.07( $\pm 1.25$ )
FedProx	67.25( $\pm 0.33$ )	54.04( $\pm 1.28$ )	53.62( $\pm 0.70$ )	54.96( $\pm 1.16$ )
FedPHP	67.16( $\pm 0.38$ )	54.23( $\pm 1.16$ )	53.37( $\pm 0.47$ )	54.86( $\pm 1.42$ )
APPLE	69.02( $\pm 0.42$ )	60.11( $\pm 1.45$ )	54.14( $\pm 1.16$ )	55.84( $\pm 0.76$ )
FedBN	67.16( $\pm 0.68$ )	54.21( $\pm 1.07$ )	53.48( $\pm 0.79$ )	54.92( $\pm 0.82$ )
SCAFFOLD	68.74( $\pm 1.03$ )	66.43( $\pm 0.58$ )	55.79( $\pm 1.30$ )	58.71( $\pm 0.84$ )
DBE	68.46( $\pm 1.05$ )	57.89( $\pm 0.75$ )	53.86( $\pm 0.58$ )	55.76( $\pm 0.95$ )
<b>Ours</b>	<b>74.91(<math>\pm 0.54</math>)</b>	<b>81.09(<math>\pm 1.31</math>)</b>	<b>86.81(<math>\pm 1.13</math>)</b>	<b>79.43(<math>\pm 1.15</math>)</b>

enabling faster convergence in settings with limited communication resources.

**Anomaly Detection.** As shown in Table 1, the performance of FedDyMem is evaluated across six datasets and compared with a set of baseline models. Conventional federated learning methods such as FedAvg, FedProx, and FedPHP show similar performance, typically outperforming the Local, but remaining below 65% AUROC on most datasets (e.g., 64% on Wafer). APPLE and FedBN show improvements over FedAvg-like methods (e.g., 65.92% AUROC on Wafer for APPLE), but their effectiveness decreases on more challenging datasets such as Brain, where AUROC remains below 51%. SCAFFOLD achieves relatively better results (e.g., 72.52% on X-ray), but provides limited gains on PCB, Brain, and MPDD. Similarly, DBE shows incremental improvements across all benchmarks but fails to match our method. In contrast, our proposed approach consistently achieves the highest I-AUROC scores across all six anomaly detection benchmarks. Specifically, our method achieves 71.96% for Wafer, 83.34% for PCB, 99.24% for MVTec, 83.93% for MPDD, 89.27% for Brain, and 80.30% for X-ray.

**Anomaly Localization.** As shown in Table 2 and Table 3, we evaluate the abnormal localization performance on four datasets (Wafer, PCB, MVTec, and MPDD), as the Brain and X-ray

do not provide region-level labels. To measure both detection capability and localization accuracy, each method is evaluated using two metrics, P-AUROC and PRO. The baseline method Local exhibits the lowest overall performance, with approximately 58.27% in P-AUROC and 47.76% in PRO on the Wafer dataset, and similar results across the other datasets. This proves that there is distribution bias in the raw dataset. For the federated learning approaches, FedAvg, FedProx, and FedPHP demonstrate closely aligned performance improvements. APPLE delivers further performance gains, achieving a P-AUROC of up to 69.88% on the Wafer dataset. In contrast, our proposed method achieves superior performance across all evaluated datasets and metrics. These consistent and robust improvements highlight the effectiveness and adaptability of our approach in tackling federated anomaly localization tasks across diverse application scenarios.

## 6.4 Ablation Study

**Impact of Local Training Epochs.** Fig. 9 illustrates the impact of varying the number of local training epochs ( $E$ ) on the performance of federated learning across all datasets. A clear trend emerges where increasing  $E$  generally results in a performance decline. For example, in the Wafer dataset, accuracy drops from 71.96% at  $E = 1$

**Table 4** Ablation study of structure for FedDyMem.

+Proj	+MG	+KM	I-AUROC (%)					P-AUROC (%)				
			Wafer	PCB	MVTec	MPDD	Brain	X-ray	Wafer	PCB	MVTec	MPDD
-	-	-	67.69	69.58	85.86	70.41	69.03	68.92	70.23	83.23	85.22	94.19
✓	-	-	68.93	74.10	87.27	78.28	74.95	72.71	74.29	89.26	90.84	95.77
✓	✓	-	70.96	81.26	92.76	81.05	85.94	78.12	77.01	94.97	96.10	97.96
✓	✓	✓	<b>71.96</b>	<b>83.34</b>	<b>99.24</b>	<b>83.93</b>	<b>89.27</b>	<b>80.30</b>	<b>78.40</b>	<b>96.03</b>	<b>97.04</b>	<b>98.97</b>

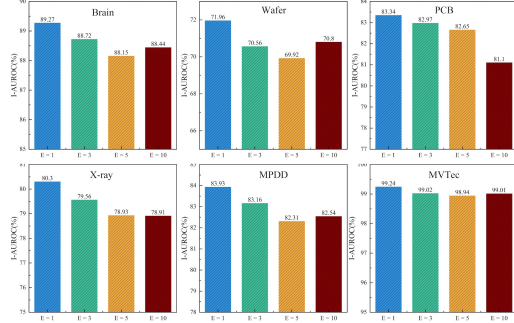


**Fig. 9** Impact of different local epochs on clients.

to 69.92% at  $E = 5$ . Similarly, the PCB dataset demonstrates a decrease in performance, with accuracy falling from 83.34% at  $E = 1$  to 82.65% at  $E = 5$ . MPDD, Brain, and X-ray also exhibit gradual performance degradation with higher  $E$  values. This phenomenon can be attributed to the heterogeneous data distribution across clients. As the number of local training epochs increases, the local models tend to overfit their respective client datasets, leading to a decrease in the effectiveness of the globally aggregated memory features.

**Effect of Projection Layer.** The ablation study presented in Table 4 shows the significant impact of incorporating a projection layer (Proj) on the performance of the proposed FedDyMem framework. The baseline configuration used for comparison consists of memory-reduction and memory feature average aggregation mechanisms, without additional architectural enhancements. Specifically, introducing the projection layer improves both I-AUROC and P-AUROC metrics across all datasets. For example, the I-AUROC for Wafer increases from 67.69% to 68.93%, and the P-AUROC improves from 70.23% to 74.29%. These results demonstrate that the projection layer effectively enhances feature representations.

**Effect of Memory Generator.** The integration of the memory generator (MG) significantly improves the anomaly detection performance of

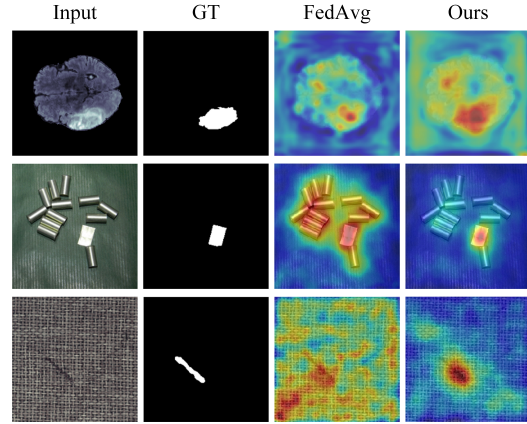


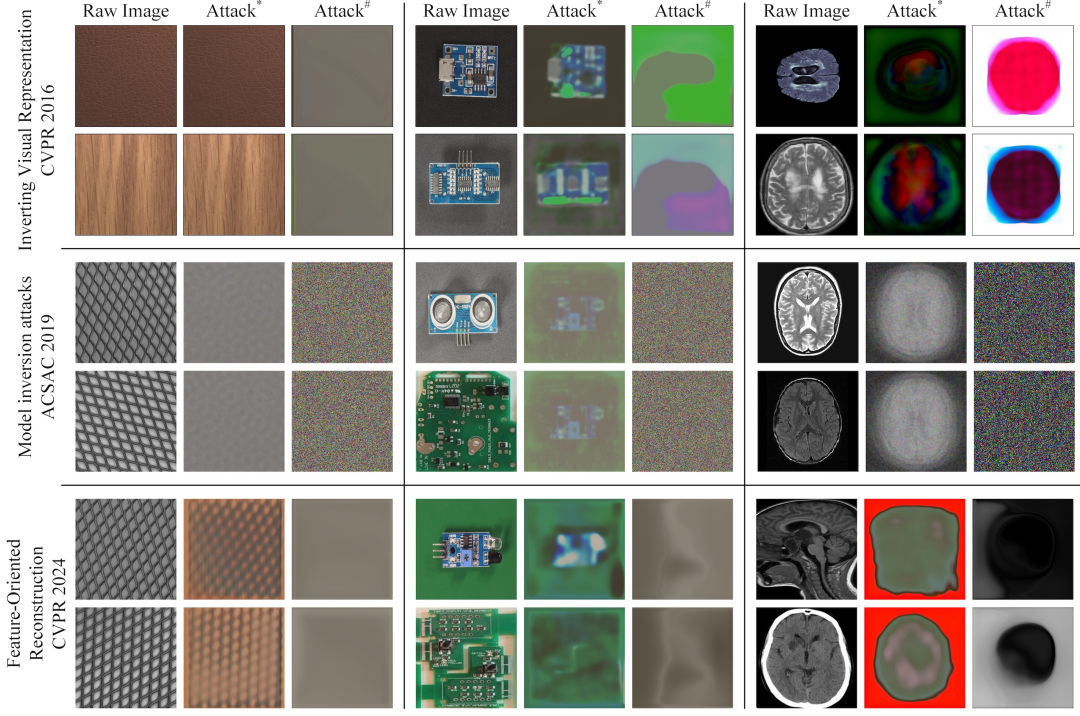
**Fig. 10** Qualitative comparison of FedAvg and our proposed method. The results were obtained from a randomly selected client using a global memory bank.

FedDyMem across different datasets. For example, the memory generator increases the I-AUROC from 68.93% to 70.96% on the wafer dataset and from 74.10% to 81.26% on the PCB dataset. A similar trend is observed for P-AUROC, with increases from 74.29% to 77.01% on Wafer and from 89.26% to 94.97% on PCB. These improvements demonstrate the ability of the memory generator to effectively refine feature representations.

**Effect of K-means.** The addition of  $K$ -means (KM) to the FedDyMem framework resulted in a consistent improvement across all evaluated metrics. When combined with the projection layer and memory generator,  $K$ -means further improves I-AUROC, achieving increases such as from 70.96% to 71.96% for Wafer and from 81.26% to 83.34% for PCB. Similarly, P-AUROC improves significantly with values such as Wafer from 77.01% to 78.40% and PCB from 94.97% to 96.03%.

## 6.5 Qualitative Results

Fig. 10 provides a qualitative comparison of the prediction results between FedAvg and the proposed FedDyMem method under an identical



\* indicates the attack input is the original feature; # indicates the attack input is the feature after memory-reduce

**Fig. 11** Qualitative reconstruction results before and after applying the proposed memory-reduce operation on MVTec, PCB, and Brain.

experimental setting. The FedDyMem approach exhibits a notable improvement in prediction quality, with substantially fewer noisy regions evident in the results. Following the methodology in (Lee et al. (2022)), the anomaly score heatmaps are upsampled to match the spatial resolution of the input image and subsequently refined using Gaussian filtering with  $\sigma = 4$ , ensuring smoother and more coherent boundaries. Furthermore, min-max normalization is applied to standardize the range of anomaly scores, facilitating clearer visualization and interpretation of the results.

## 6.6 Privacy Verification

To evaluate the privacy-preserving capability of FedDyMem, we conducted reconstruction attack experiments under representative adversarial settings. In these experiments, we considered the threat scenario in which an attacker attempts to recover original input images from the memory features exchanged between clients and the server. We applied three widely used attack methods, including the deconvolution-based inverting

method (Dosovitskiy and Brox (2016)), the collaborative inference attack method (He et al. (2019)), and the stealthy feature-oriented reconstruction attack (Xu et al. (2024)). We evaluated the quality of the reconstructed images using three established metrics. The Structural Similarity Index (SSIM) and Peak Signal-to-Noise Ratio (PSNR) assess the perceptual and signal-level fidelity between the reconstructed and original images. The Fréchet Inception Distance (FID) measures the semantic distance in a high-level feature space and reflects how closely the generated samples resemble raw data. A higher SSIM and PSNR indicate stronger reconstruction fidelity and thus greater privacy leakage, while a lower FID suggests a closer match in feature distribution to the original images.

Table 5 presents the performance of each attack method across three datasets before and after applying the memory-reduce. Across all attack settings, memory-reduce consistently degrades both the reconstruction quality and the success rate of the adversaries. Specifically, we observe lower SSIM and PSNR values and

**Table 5** Quantitative reconstruction attack results before and after memory-reduce.

Attack Methods	Dataset	+Memory-Reduce	SSIM	PSNR	FID
Deconvolution Inverting Method	MVTec	-	0.6350	25.9003	246.9916
		✓	0.2088	17.4787	415.9250
	PCB	-	0.5213	25.8625	281.5855
		✓	0.3379	12.1827	358.7053
	Brain	-	0.2273	11.0985	300.5543
		✓	0.0872	2.8752	338.1136
Collaborative inference attack	MVTec	-	0.0928	15.5441	300.9797
		✓	0.0179	11.4840	350.8446
	PCB	-	0.4860	13.9388	313.1274
		✓	0.0178	10.7200	418.3834
	Brain	-	0.1218	11.2046	365.9037
		✓	0.0038	6.5987	396.2980
Feature Reconstruction Attack	MVTec	-	0.2094	16.2157	231.2310
		✓	0.0869	15.3695	326.0596
	PCB	-	0.5391	17.4453	327.5368
		✓	0.2073	14.2317	370.4590
	Brain	-	0.5629	20.2312	240.1137
		✓	0.1558	7.8485	352.5879

higher FID scores after memory-reduce is applied, indicating reduced visual similarity and semantic fidelity between reconstructed and original images. Moreover, the ASR drops to 0% in all but one case, where it is reduced from 28.57% to 5.23%, highlighting the strong effectiveness of memory-reduce in mitigating reconstruction attacks. In addition to the quantitative results, we present qualitative comparisons in Fig. 11, which visualizes representative reconstructed samples under different settings. The reconstructions before applying memory-reduce retain identifiable structure or texture information from the original images, especially in regions with distinct contours. In contrast, after memory-reduce is applied, the reconstructed images exhibit significant degradation in visual fidelity. The overall shape, content, and fine-grained patterns become vague or distorted, demonstrating the effectiveness of memory-reduce in suppressing reconstruction attacks.

## 7 Conclusion

In this article, we propose an efficient federated learning with dynamic memory and memory-reduce, called FedDyMem to address the federated UAD problem. To tackle the challenges posed by multi-client data distribution bias in

real-world industrial and medical scenarios, FedDyMem introduces a memory generator and a loss function based on distance metrics to dynamically generate high-quality memory banks. To enhance both communication efficiency and privacy protection, a memory-reduce method is incorporated to compress memory features and reduce their mutual information with raw data. During the aggregation phase, K-means is employed on the server to mitigate ambiguity and confusion across memory banks from different clients. Extensive experimental results demonstrate that the proposed method significantly outperforms existing baselines. Future work will focus on optimizing the model heterogeneity adaptation to further enhance the scalability and generalization of the proposed framework.

## References

Almanifi ORA, Chow CO, Tham ML, et al (2023) Communication and computation efficiency in federated learning: A survey. *Internet of Things* 22:100742

Alsulaimawi Z (2024) Federated learning with privacy-preserving active learning: A min-max mutual information approach. In: 2024 International Conference on Artificial Intelligence in Information and Communication (ICAIIC), IEEE, pp 503–508

Bae J, Lee JH, Kim S (2023) Pni: Industrial anomaly detection using position and neighborhood information. In: Proceedings of the IEEE/CVF International Conference on Computer Vision, pp 6373–6383

Bai H, Mou S, Likhomanenko T, et al (2023) Vision datasets: A benchmark for vision-based industrial inspection. *arXiv preprint arXiv:230607890*

Baid U, Ghodasara S, Mohan S, et al (2021) The rsna-asnr-miccai brats 2021 benchmark on brain tumor segmentation and radiogenomic classification. *arXiv preprint arXiv:210702314*

Bergmann P, Löwe S, Fauser M, et al (2018) Improving unsupervised defect segmentation by applying structural similarity to autoencoders.

arXiv preprint arXiv:180702011

Bergmann P, Fauser M, Sattlegger D, et al (2019) Mvttec ad—a comprehensive real-world dataset for unsupervised anomaly detection. In: Proceedings of the IEEE/CVF conference on computer vision and pattern recognition, pp 9592–9600

Cai Y, Zhang W, Chen H, et al (2024) Medi-anomaly: A comparative study of anomaly detection in medical images. arXiv preprint arXiv:240404518

Cao S, Liu S, Yang Y, et al (2025) A hybrid and efficient federated learning for privacy preservation in iot devices. *Ad Hoc Networks* 170:103761

Cohen N, Hoshen Y (2020) Sub-image anomaly detection with deep pyramid correspondences. arXiv preprint arXiv:200502357

Dai S, Wu Y, Li X, et al (2024) Generating and reweighting dense contrastive patterns for unsupervised anomaly detection. In: Proceedings of the AAAI Conference on Artificial Intelligence, pp 1454–1462

Dai Y, Chen Z, Li J, et al (2023) Tackling data heterogeneity in federated learning with class prototypes. In: Proceedings of the AAAI Conference on Artificial Intelligence, pp 7314–7322

Defard T, Setkov A, Loesch A, et al (2021) Padim: a patch distribution modeling framework for anomaly detection and localization. In: International Conference on Pattern Recognition, Springer, pp 475–489

Dosovitskiy A, Brox T (2016) Inverting visual representations with convolutional networks. In: Proceedings of the IEEE conference on computer vision and pattern recognition, pp 4829–4837

Han S, Park S, Wu F, et al (2022) Fedx: Unsupervised federated learning with cross knowledge distillation. In: European Conference on Computer Vision, Springer, pp 691–707

He K, Zhang X, Ren S, et al (2016) Deep residual learning for image recognition. In: Proceedings of the IEEE conference on computer vision and pattern recognition, pp 770–778

He Z, Zhang T, Lee RB (2019) Model inversion attacks against collaborative inference. In: Proceedings of the 35th annual computer security applications conference, pp 148–162

Huang W, Ye M, Shi Z, et al (2023) Rethinking federated learning with domain shift: A prototype view. In: 2023 IEEE/CVF Conference on Computer Vision and Pattern Recognition (CVPR), IEEE, pp 16312–16322

Jezek S, Jonak M, Burget R, et al (2021) Deep learning-based defect detection of metal parts: evaluating current methods in complex conditions. In: 2021 13th International congress on ultra modern telecommunications and control systems and workshops (ICUMT), IEEE, pp 66–71

Ji C, Heusdens R, Maag S, et al (2025) Re-evaluating privacy in centralized and decentralized learning: An information-theoretical and empirical study. In: ICASSP 2025-2025 IEEE International Conference on Acoustics, Speech and Signal Processing (ICASSP), IEEE, pp 1–5

Jiang J, Zhu J, Bilal M, et al (2022) Masked swin transformer unet for industrial anomaly detection. *IEEE Transactions on Industrial Informatics* 19(2):2200–2209

Jin Y, Liu Y, Chen K, et al (2023) Federated learning without full labels: A survey. arXiv preprint arXiv:230314453

Karimireddy SP, Kale S, Mohri M, et al (2020) Scaffold: Stochastic controlled averaging for federated learning. In: International conference on machine learning, PMLR, pp 5132–5143

Kermany DS, Goldbaum M, Cai W, et al (2018) Identifying medical diagnoses and treatable diseases by image-based deep learning. *cell* 172(5):1122–1131

Kim H, Kwak Y, Jung M, et al (2023) Protofl: Unsupervised federated learning via prototypical distillation. In: Proceedings of the

IEEE/CVF International Conference on Computer Vision, pp 6470–6479

Lee JC, Kim T, Park E, et al (2025) Continuous memory representation for anomaly detection. In: European Conference on Computer Vision, Springer, pp 438–454

Lee S, Lee S, Song BC (2022) Cfa: Coupled-hypersphere-based feature adaptation for target-oriented anomaly localization. *IEEE Access* 10:78446–78454

Lei T, Chen S, Wang B, et al (2025) Adapted-moe: Mixture of experts with test-time adaption for anomaly detection. In: International Conference on Intelligent Computing, Springer, pp 427–441

Li J, Li C, Fan J, et al (2023a) Online distributed stochastic gradient algorithm for non-convex optimization with compressed communication. *IEEE Transactions on Automatic Control*

Li J, Li F, Zhu L, et al (2023b) Prototype-guided knowledge transfer for federated unsupervised cross-modal hashing. In: Proceedings of the 31st ACM International Conference on Multimedia, pp 1013–1022

Li Q, Wen Z, Wu Z, et al (2021a) A survey on federated learning systems: Vision, hype and reality for data privacy and protection. *IEEE Transactions on Knowledge and Data Engineering* 35(4):3347–3366

Li T, Sahu AK, Talwalkar A, et al (2020a) Federated learning: Challenges, methods, and future directions. *IEEE signal processing magazine* 37(3):50–60

Li T, Sahu AK, Zaheer M, et al (2020b) Federated optimization in heterogeneous networks. *Proceedings of Machine learning and systems* 2:429–450

Li T, Sahu AK, Zaheer M, et al (2020c) Federated optimization in heterogeneous networks. *Proceedings of Machine learning and systems* 2:429–450

Li X, Jiang M, Zhang X, et al (2021b) Fedbn: Federated learning on non-iid features via local batch normalization. *arXiv preprint arXiv:210207623*

Li XC, Zhan DC (2021) Fedrs: Federated learning with restricted softmax for label distribution non-iid data. In: Proceedings of the 27th ACM SIGKDD conference on knowledge discovery & data mining, pp 995–1005

Li XC, Zhan DC, Shao Y, et al (2021c) Fedphp: Federated personalization with inherited private models. In: Joint European Conference on Machine Learning and Knowledge Discovery in Databases, Springer, pp 587–602

Li XC, Xu YC, Song S, et al (2022) Federated learning with position-aware neurons. In: Proceedings of the IEEE/CVF Conference on Computer Vision and Pattern Recognition, pp 10082–10091

Li Z, Lin Z, Shao J, et al (2024a) Fedcir: Client-invariant representation learning for federated non-iid features. *IEEE Transactions on Mobile Computing*

Li Z, Sun Y, Shao J, et al (2024b) Feature matching data synthesis for non-iid federated learning. *IEEE Transactions on Mobile Computing*

Liang Y, Zhang J, Zhao S, et al (2023) Omni-frequency channel-selection representations for unsupervised anomaly detection. *IEEE Transactions on Image Processing*

Liao X, Liu W, Chen C, et al (2024) Rethinking the representation in federated unsupervised learning with non-iid data. In: Proceedings of the IEEE/CVF Conference on Computer Vision and Pattern Recognition, pp 22841–22850

Liu R, Lehman J, Molino P, et al (2018) An intriguing failing of convolutional neural networks and the coordconv solution. *Advances in neural information processing systems* 31

Lubana ES, Tang CI, Kawsar F, et al (2022) Orchestra: Unsupervised federated learning via globally consistent clustering. In: Proc. International Conference on Machine Learning

Luo J, Wu S (2022) Adapt to adaptation: Learning personalization for cross-silo federated learning. In: IJCAI: proceedings of the conference, NIH Public Access, p 2166

Maaten Lvd, Hinton G (2008) Visualizing data using t-sne. *Journal of machine learning research* 9(Nov):2579–2605

McMahan B, Moore E, Ramage D, et al (2017) Communication-efficient learning of deep networks from decentralized data. In: Artificial intelligence and statistics, PMLR, pp 1273–1282

Nguyen DC, Ding M, Pathirana PN, et al (2021) Federated learning for covid-19 detection with generative adversarial networks in edge cloud computing. *IEEE Internet of Things Journal* 9(12):10257–10271

Nguyen HQ, Lam K, Le LT, et al (2022) Vindr-cxr: An open dataset of chest x-rays with radiologist's annotations. *Scientific Data* 9(1):429

Roth K, Pemula L, Zepeda J, et al (2022) Towards total recall in industrial anomaly detection. In: Proceedings of the IEEE/CVF conference on computer vision and pattern recognition, pp 14318–14328

Saha S, Hota A, Chattpadhyay AK, et al (2024) A multifaceted survey on privacy preservation of federated learning: progress, challenges, and opportunities. *Artificial Intelligence Review* 57(7):184

Salehi M, Sadjadi N, Baselizadeh S, et al (2021) Multiresolution knowledge distillation for anomaly detection. In: Proceedings of the IEEE/CVF conference on computer vision and pattern recognition, pp 14902–14912

Shlezinger N, Chen M, Eldar YC, et al (2020) Uveqfed: Universal vector quantization for federated learning. *IEEE Transactions on Signal Processing* 69:500–514

Tan Q, Li Q, Zhao Y, et al (2024) Defending against data reconstruction attacks in federated learning: An information theory approach. In: 33rd USENIX Security Symposium (USENIX Security 24), pp 325–342

Tan Y, Long G, Liu L, et al (2022a) Fedproto: Federated prototype learning across heterogeneous clients. In: Proceedings of the AAAI Conference on Artificial Intelligence, pp 8432–8440

Tan Y, Long G, Ma J, et al (2022b) Federated learning from pre-trained models: A contrastive learning approach. *Advances in neural information processing systems* 35:19332–19344

Wang X, Peng Y, Lu L, et al (2017) Chestx-ray8: Hospital-scale chest x-ray database and benchmarks on weakly-supervised classification and localization of common thorax diseases. In: Proceedings of the IEEE conference on computer vision and pattern recognition, pp 2097–2106

Wu Y, Desrosiers C, Chaddad A (2024) Facmic: Federated adaptative clip model for medical image classification. In: International Conference on Medical Image Computing and Computer-Assisted Intervention, Springer, pp 531–541

Xie G, Wang J, Liu J, et al (2024) Im-iad: Industrial image anomaly detection benchmark in manufacturing. *IEEE Transactions on Cybernetics*

Xu J, Wang H (2020) Client selection and bandwidth allocation in wireless federated learning networks: A long-term perspective. *IEEE Transactions on Wireless Communications* 20(2):1188–1200

Xu X, Yang M, Yi W, et al (2024) A stealthy wrongdoer: Feature-oriented reconstruction attack against split learning. In: Proceedings of the IEEE/CVF conference on computer vision and pattern recognition, pp 12130–12139

Yang G, Yang Z, Cui S, et al (2024) Clustering federated learning for wafer defects classification on statistical heterogeneous data. *IEEE Transactions on Instrumentation and Measurement*

Yang Q, Chen Z, Peng Z, et al (2025) Relation-guided versatile regularization for federated semi-supervised learning. *International Journal of Computer Vision* pp 1–15

Yang Z, Bao W, Yuan D, et al (2022) Federated learning with nesterov accelerated gradient. *IEEE Transactions on Parallel and Distributed Systems* 33(12):4863–4873

You Z, Cui L, Shen Y, et al (2022) A unified model for multi-class anomaly detection. *Advances in Neural Information Processing Systems* 35:4571–4584

Zavrtanik V, Kristan M, Skočaj D (2021) Draem-a discriminatively trained reconstruction embedding for surface anomaly detection. In: *Proceedings of the IEEE/CVF international conference on computer vision*, pp 8330–8339

Zhang C, Xie Y, Chen T, et al (2024a) Prototype similarity distillation for communication-efficient federated unsupervised representation learning. *IEEE Transactions on Knowledge and Data Engineering*

Zhang H, Li C, Dai W, et al (2023) Fedcr: Personalized federated learning based on across-client common representation with conditional mutual information regularization. In: *International Conference on Machine Learning*, PMLR, pp 41314–41330

Zhang J, Hua Y, Cao J, et al (2024b) Eliminating domain bias for federated learning in representation space. *Advances in Neural Information Processing Systems* 36

Zhang J, Liu Y, Hua Y, et al (2024c) Fedtgp: Trainable global prototypes with adaptive-margin-enhanced contrastive learning for data and model heterogeneity in federated learning. In: *Proceedings of the AAAI Conference on Artificial Intelligence*, pp 16768–16776

Zhang R, Li H, Tian L, et al (2024d) Vertical federated learning across heterogeneous regions for industry 4.0. *IEEE Transactions on Industrial Informatics*

Zhao Y, Li M, Lai L, et al (2018) Federated learning with non-iid data. *arXiv preprint arXiv:180600582*

Zhao Y, Liu Q, Liu P, et al (2024) Medical federated model with mixture of personalized and shared components. *IEEE Transactions on Pattern Analysis and Machine Intelligence*

Zhou T, Yuan Y, Wang B, et al (2024) Federated feature augmentation and alignment. *IEEE Transactions on Pattern Analysis and Machine Intelligence*

Zhuang W, Gan X, Wen Y, et al (2021) Collaborative unsupervised visual representation learning from decentralized data. In: *2021 IEEE/CVF International Conference on Computer Vision*. IEEE, pp 4892–4901

Zou Y, Jeong J, Pemula L, et al (2022) Spot-the-difference self-supervised pre-training for anomaly detection and segmentation. In: *European Conference on Computer Vision*, Springer, pp 392–408